CHALMERS
UNIVERSITY OF TECHNOLOGY

Mitigation of transient torque reversals in indirect drive wind turbine drivetrains

Downloaded from: https://research.chalmers.se, 2026-04-06 07:12 UTC

Citation for the original published paper (version of record):
Sarkar, S., Johansson, H., Berbyuk, V. (2023). Mitigation of transient torque reversals in indirect drive wind turbine drivetrains. Wind Energy, 26: 803-825. http://dx.doi.org/10.1002/we.2842

N.B. When citing this work, cite the original published paper.

research.chalmers.se offers the possibility of retrieving research publications produced at Chalmers University of Technology. It covers all kind of research output: articles, dissertations, conference papers, reports etc. since 2004. research.chalmers.se is administrated and maintained by Chalmers Library

(article starts on next page)

Check for updates

Received: 10 January 2023 | Revised: 31 March 2023 | Accepted: 15 May 2023

DOI: 10.1002/we.2842

RESEARCH ARTICLE

WILEY

Mitigation of transient torque reversals in indirect drive wind turbine drivetrains

Saptarshi Sarkar | **Håkan Johansson** | **Viktor Berbyuk**

Department of Mechanics and Maritime Sciences, Chalmers University of Technology, Gothenburg, Sweden

Correspondence
Saptarshi Sarkar, Department of Mechanics and Maritime Sciences, Chalmers University of Technology, Gothenburg, Sweden.
Email: ssarkar@chalmers.se

Funding information
Swedish Wind Power Technology Centre (SWPTC); Swedish Energy Agency, Grant/Award Number: P2018-32591

Abstract

Bearing failure in wind turbine gearboxes is one of the significant sources of downtime. While it is well-known that bearing failures cause the largest downtime, the failure cause(s) is often elusive. The bearings are designed to satisfy their rolling contact fatigue (RCF) life. However, they often undergo sudden and rapid failure within a few years of operation. It is well-known that these premature failures are attributed to surface damages such as white surface flaking (WSF), white etching cracks (WECs) and axial cracks. In that regard, transient torque reversals (TTRs) in the drivetrain have emerged as one of the primary triggers of surface damage, as explained in this paper. The risk associated with TTRs motivates the need to mitigate TTRs arising in the drivetrain due to various transient events. This paper investigates three TTR mitigation methods. First, two existing devices, namely, the torsional tuned mass damper and the asymmetric torque limiter, are studied to demonstrate their TTR mitigation capabilities. Then, a novel idea of open-loop high-speed shaft mechanical brake control is proposed. The results presented here show that while the torsional tuned mass damper and the asymmetric torque limiter can improve the torsional vibration characteristics of the drivetrain, they cannot mitigate TTRs in terms of eliminating the bearing slip risk associated with TTRs. However, the novel approach proposed here can mitigate TTRs both in terms of improving the torque characteristic in the high-speed shaft and reducing the risk of bearing slip by actuating the high-speed shaft brake at the onset of the transient event. Furthermore, the control method is capable of mitigating TTRs with the mechanical limitations of a pneumatic actuator in terms of bandwidth and initial dead time applied to it. This novel approach allows the wind turbines to protect the gearbox bearings from TTRs using the existing hardware on the turbine.

KEYWORDS
asymmetric torque limiter, brake control, SIMPACK gearbox model, torsional tuned mass damper, transient torque reversals, wind turbine

1 | INTRODUCTION

Today, wind power is among the most important contributors to the cleaner and greener energy drive. In 2021, 93.6 GW of new wind power was installed globally bringing the cumulative wind power capacity to 837 GW, showing a year-over-year (YoY) growth of 12%.[1] New installations in

This is an open access article under the terms of the Creative Commons Attribution License, which permits use, distribution and reproduction in any medium, provided the original work is properly cited.
© 2023 The Authors. *Wind Energy* published by John Wiley & Sons Ltd.

10991824, 0, Downloaded from https://onlinelibrary.wiley.com/doi/10.1002/we.2842 by Chalmers University Of Technology, Wiley Online Library on [19/06/2023]. See the Terms and Conditions (https://onlinelibrary.wiley.com/terms-and-conditions) on Wiley Online Library for rules of use; OA articles are governed by the applicable Creative Commons License

the onshore wind market reached 72.5 GW, 18% lower than the previous year due to a slowdown in China and the United States due to COVID-19; however, is still the second-best year in its history. The wind energy market is expected to pick up again postpandemic. A total of 21.1 GW offshore wind was commissioned in 2021 making it the best-ever year for offshore wind. This is three times more than the previous year. New offshore installations represented 22.5% of all new installations in 2021, helping bring the world's total offshore capacity to 57 GW, which is 7% of global installations. The CAGR (Compound Annual Growth Rate) for onshore wind in the next 5 years is 6.1%, with average annual installations of 93.3 GW. In total, 466 GW is likely to be built in 2022–2026. The CAGR for offshore wind in the next 5 years is 8.3%.[1] This expected growth in the wind energy market is also supported by Fortune Business Insights[2] report that the global wind turbine gearbox market is expected to grow from $19.33 billion in 2021 to $32.55 billion by 2028 at a CAGR of 7.7% in the forecast period, 2021–2028. Thus, indirect drive (geared) wind turbines will play a major role in the future wind energy market. Kaa et al[3] also present a similar outlook as they have reported that both the gearbox (indirect drive) wind turbine and the direct drive wind turbine have their merits, and in markets, such as wind energy, the two designs can co-exist. There does not seem to be a clear winner.

To achieve the projected cumulative growth in wind energy, it is necessary to improve their lifetime by developing more robust and resilient wind turbines. One major challenge is reducing downtime occurring from the failure of different parts of the turbine, where gearbox failures typically result in the longest turbine downtime.[4,5] Although the failure rates of the gearboxes are low compared with the electric and control systems, the mechanical components account for more than 75% of the total downtime.[5] It is also important to note that drivetrain module repair costs are typically more expensive than the electrical/control components due to crane costs. The main contributors to gearbox failures are bearings $\approx 70\%$ followed by gears $\approx 26\%$, and other failures constitute the remaining $\approx 4\%$.[6] Forty-eight percent of all failures are attributed to high-speed shaft bearings, followed by 13% to the intermediate shaft bearings and 7% to the planetary bearings.[6] All other component failures (gears and others) account for the remaining 32%. Therefore, it is clear that bearing failures contribute greatly to wind turbine gearboxes' unpredictable and premature failure. Surface damages on high-speed shaft bearings, planetary bearings and intermediate speed shaft bearings mainly limit the service life.[7] Bearings are designed to satisfy a minimum rolling contact fatigue (RFC) life. However, failures within a few years of operation are observed because smearing/scuffing, white etching cracks (WECs) and axial cracking failure modes differ from the classical RCF failure mode.

Two prevalent surface failure modes in multimegawatt wind turbine gearbox bearings are as smearing/scuffing[8] and white structure flaking (WSF).[9] Slip is often considered as being essential to the formation of white etching areas (WEAs)[9] and smearing damage.[8] Slip can independently lead to either smearing/scuffing damage and WSF or severely promote WEA formation.[10] Once an event initiates subsurface WEA formations, normal rolling action of the bearing can initiate cracks at the junction of the inclusion-like areas.[11] The crack inevitably propagates to the surface and becomes a WEC, which grows axially across the raceway and causes premature bearing failures.[11] The drivers and mechanisms of the onset of smearing/scuffing or white etching surface formation are still highly contested. Evans[9] presents an extensive review of operational modes, drivers and mechanics that lead to three types of WECs and axial cracks: (a) hydrogen-induced, (b) electro-thermal stress-induced and (c) mechanical stress-induced. Some of the drivers identified by researchers are hydrogen embrittlement, sliding kinematics, water contamination, low Hertzian contact pressure, electrical potential, lubricant additives and tensile hoop stress.[9,12] However, the slip and impact loading during transient torque reversals (TTRs) is suggested to be a leading candidate in causing stress-induced subsurface WEA damage as illustrated in Sharpley.[11]

In an indirect drive doubly fed induction generator (DFIG) wind turbine, the phenomenon of TTRs typically involves rapid reversals and multiple zero-crossings in the shaft torque Figure 1A. The multiple zero-crossings in shaft torque are accompanied by rapid reversals of the bearing loaded zone. This phenomenon is termed bearing load reversals (BLRs) where the bearing radial loading angle rapidly changes its sign by $\approx 180^\circ$, as shown in Figure 1B. To elaborate on the subsequent events, Figure 2 shows the formation of surface damage from TTRs. However, it must be noted that Figure 2 shows the sequence of events that arise from TTRs and does not include all drivers that lead to slip/skid and eventually to surface damage in multimegawatt wind turbine bearings.

The risk of damage associated with TTRs described above demonstrates the need to identify operational modes that lead to TTRs and consequently mitigate the damaging effect of TTRs to protect the bearings from surface damage. In a previous investigation, the authors identified that grid faults like symmetric voltage dips and emergency shutdowns lead to TTRs. Similar observations were also made by Röder et al[13,14] as they found an increased risk of smearing during grid and converter faults. To mitigate the risk associated with TTRs, three different approaches have been investigated here and their performance evaluated for symmetrical voltage dip and emergency shutdown events in a DFIG wind turbine. Among the three approaches, first, a torsional tuned mass damper (TMD) and an asymmetric torque limiter are investigated separately. Next, a novel active control of the high-speed shaft mechanical brake in an open-loop architecture has been proposed.

An important task in this process is to develop a metric that can quantify the risk associated with TTRs. Röder et al[14] used frictional power intensity (FPI) to estimate a smearing criterion indicating the risk of smearing. However, sophisticated simulation models or instrumentation is required to track indicators such as a rise in inlet temperature or a rise in FPI. In the absence of such models or instrumentation, Eatherton et al[15] used metrics such as the maximum amplitude of oscillations and maximum negative torque excursion in the high-speed shaft to quantify the damaging effect of TTRs. However, these torque measurements do not account for the BLRs described in Figure 1. Therefore, a metric is required that can account for BLRs during TTR to accurately quantify the risk associated with TTRs. To this end, a quantity termed as *slip-risk duration* is proposed to be used here. The *slip-risk duration* represents the time duration spent by the bearings in a high *slip-risk* situation. The metric is formulated by defining thresholds, exceeding which signifies an increased risk of slip. Based on the reviewed literature, the two important thresholds

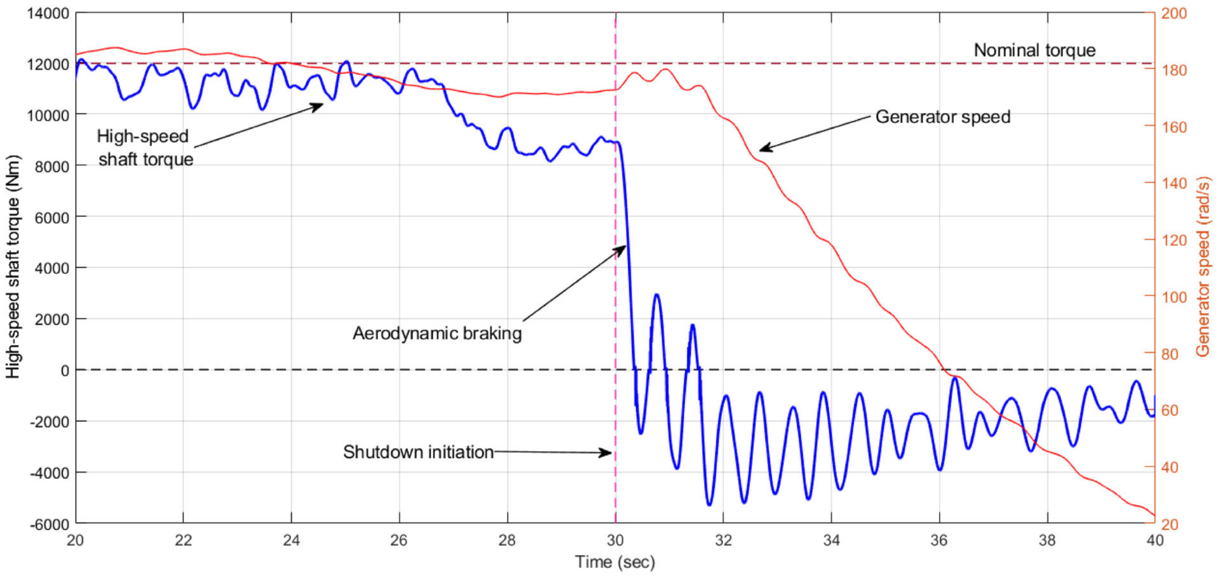

(A) High-speed shaft torque during an emergency shutdown

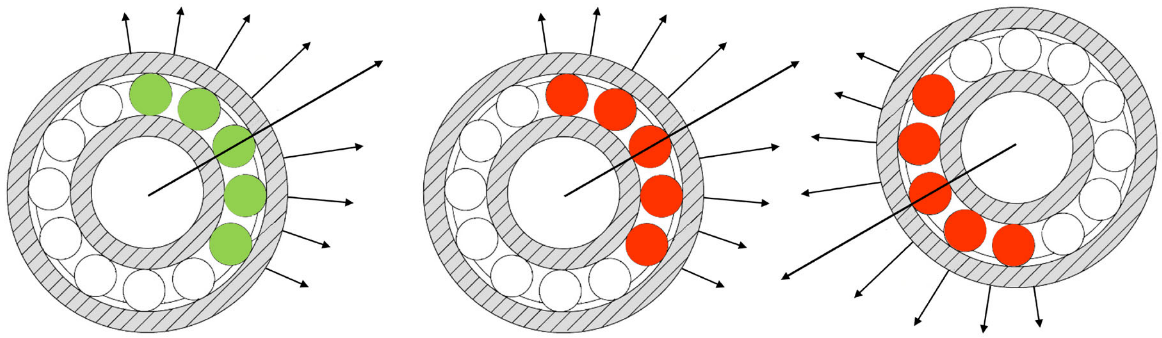

(B) Aligned (green) rollers during normal operation, misaligned (red) rollers 180° opposite of the loaded zone get suddenly loaded and unloaded repeatedly.

FIGURE 1 (A, B) Transient torque reversals during an emergency shutdown event.

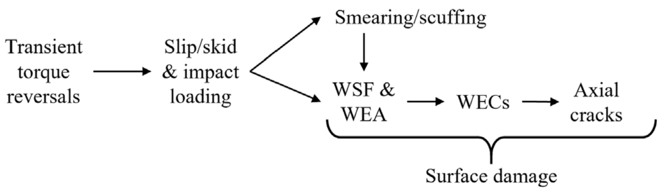

FIGURE 2 Formation of surface damage from transient torque reversals (*Note*: This diagram only shows the sequence of events that arise from transient torque reversals (TTRs) and does not include all drivers that lead to slip/skid and subsequently to surface damage in multi-megawatt wind turbine bearings.). WEA, white etching area; WEC, white etching crack; WSF, white structure flaking.

are identified as follows: (a) a critical radial bearing load, below which it can be considered that the bearings are *lightly loaded*, and (b) a critical inner-raceway speed, above which the shaft is *rotating fast*. Ideally, to formulate these thresholds, the bearing at hand must be tested using the appropriate choice of lubricant and temperature. In the lack of such experimental results, these thresholds are determined from the literature[8,16,17] and have been assumed as follows:

1. Low radial bearing forces $\leq 1\%C$ (dynamic load rating) accompanied by the sporadic and rapid reversal of radial load direction.
2. Simultaneously, the inner-raceway speed must be higher than 2.6 m/s.

10991824, 0, Downloaded from https://onlinelibrary.wiley.com/doi/10.1002/we.2842 by Chalmers University Of Technology, Wiley Online Library on [19/06/2023]. See the Terms and Conditions (https://onlinelibrary.wiley.com/terms-and-conditions) on Wiley Online Library for rules of use; OA articles are governed by the applicable Creative Commons License

The time spent by the bearings beyond these thresholds is quantified as the risk of slip/smear associated with the different transient events. The proposed metric above is based on the assumption that the amount of bearing preload is small. With substantial preload, the chosen loading threshold of 1%C should be revised. This metric, along with torque measurements like the amplitude of the maximum oscillations and maximum negative torque excursion, is used to evaluate the performance of the mitigation methods investigated and proposed in this paper.

The topic of vibration mitigation in wind turbine drivetrains has been sparsely addressed in the literature. In one of the earliest studies, Fateh et al[18] presented a nonlinear technique based on the sliding mode control theory to mitigate torsional vibrations in grid-connected DFIG-based wind turbines. The author derived a compensation torque to be superimposed onto a desired torque formulated based on a maximum power tracking algorithm. The proposed controller was able to reduce torsional vibrations in the drivetrain. Lee et al[19] investigated the use of a centrifugal pendulum absorber (CPA) to attenuate the torsional vibration in a wind turbine drivetrain showing good performance on the torsion vibration reduction for the drivetrain. Peng et al[20] put forward a vibration absorption method based on modal interaction to alleviate the whole-body vibration of the wind turbine gearbox mounted on flexible suspensions. The vibration absorber in Peng et al[20] is constructed using a servomotor and a swing rod attached to the output end of the former. However, these studies do not consider the effect of TTRs in terms of BLRs. Therefore, no conclusion can be drawn on their effect on BLRs and the induced slip risk. In this paper, we proposed a novel approach that can mitigate TTRs both in terms of improving the torque characteristic in the high-speed shaft and reducing the risk of bearing slip.

This paper is structured as follows: first, the model used for the numerical investigation is detailed in Section 2. Next, Section 3 describes the three TTR mitigation methods investigated here. In Section 4, first, the results of the torsional TMD and the asymmetric torque controller are presented. Then the results of the proposed open-loop control strategy for the high-speed shaft brake are presented. Section 4 is concluded with of comparison of the three mitigation methods. The paper ends with recommendations to mitigate TTRs in multimegawatt DFIG wind turbine drivetrains during grid faults and emergency shutdowns.

2 | GENERIC MODEL OF A 2 MW ONSHORE WIND TURBINE

A generic 2 MW wind turbine model is developed inspired by the behaviour/power production of a Vestas V90 machine. The state-of-the-art aeroelastic simulation tool OpenFAST[21] is used for aeroelastic simulations of the wind turbine in this paper. The generic 2 MW wind turbine model is developed by downscaling the NREL 5 MW reference wind turbine[22] guided by Vestas V90-2.0[23] power curve and the available SCADA data. The generic turbine has a cut-in wind speed of 3.5 m/s, reaches its maximum power at 13 m/s and automatically shuts down if the hub-height wind speed is higher than 25 m/s. The drivetrain of the turbine consists of a three-stage gearbox composed of one planetary stage and two parallel stages and a DFIG. During an emergency shutdown, aerodynamic braking only is used to bring the turbine to a standstill. The 2 MW wind turbine specifications used in this paper are summarized in Table A1. The generator power versus wind speed and generator torque versus generator speed characteristics are shown in Figure 3. It must be noted that the generic 2 MW wind turbine model used here is not aimed to be an exact representation of a Vestas V90 wind turbine but serves as a baseline 2 MW wind turbine model that mimics the performance of a Vestas V90-2.0[23] turbine. The coupled numerical model used in this paper comprises a multibody dynamic model of the wind turbine drivetrain developed in SIMPACK, a dynamic model of the DFIG and the associated control systems developed in Simulink®. Furthermore, these two models are coupled with the wind turbine simulator OpenFAST to offer a high-fidelity numerical model of the coupled electromechanical system. The models are briefed in the following.

2.1 | Multibody drivetrain model in SIMPACK

A model of the drivetrain has been developed using the multibody system simulation software SIMPACK.[24] The four-point drivetrain has a three-stage gearbox with one planetary stage and two helical stages. The main shaft is supported by two spherical bearings, and the high-speed shaft (HSS) is supported by three bearings as shown in Figure 4. The main bearings are connected directly to the bedplate, whereas all other bearings are connected to the gearbox housing. The downwind end of the high-speed shaft is connected directly to the generator. The structural members of the drivetrain are modelled as rigid bodies. All gears are modelled using the primitive `25: Gear Wheel` from the SIMPACK library using the data presented in Table A2. The SIMPACK Force Element `225: Gear Pair` is used for a detailed description of all tooth contact between two meshing gear wheels with involute geometry. The `225: Gear Pair` element allows multiple tooth meshing, whereby all the individual tooth pairing contacts along the line of action are calculated. The resulting overall transfer forces and torques are calculated by adding the individual forces at each contacting tooth. The `225: Gear Pair` element is capable of estimating the time-varying meshing forces between two gear wheels. The shaft(s) flexibility is modelled using the SIMPACK Force Element `43: Bushing Cmp` in SIMPACK. In this study, the torsional stiffness of the shafts is used. The bearings are modelled using Force Element `88: Rolling Bearing` in SIMPACK with the data presented in Table A3.

10991824, 0, Downloaded from https://onlinelibrary.wiley.com/doi/10.1002/we.2842 by Chalmers University Of Technology, Wiley Online Library on [19/06/2023]. See the Terms and Conditions (https://onlinelibrary.wiley.com/terms-and-conditions) on Wiley Online Library for rules of use; OA articles are governed by the applicable Creative Commons License

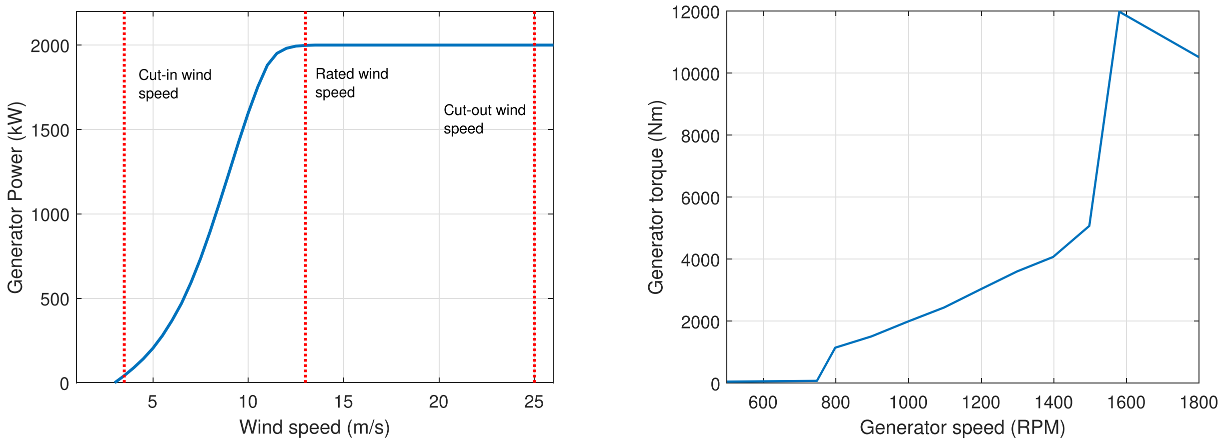

(A) Generator power vs wind speed **(B)** Generator torque vs generator speed

FIGURE 3 (A, B) Generator torque, speed and power characteristics of the generic 2 MW wind turbine.

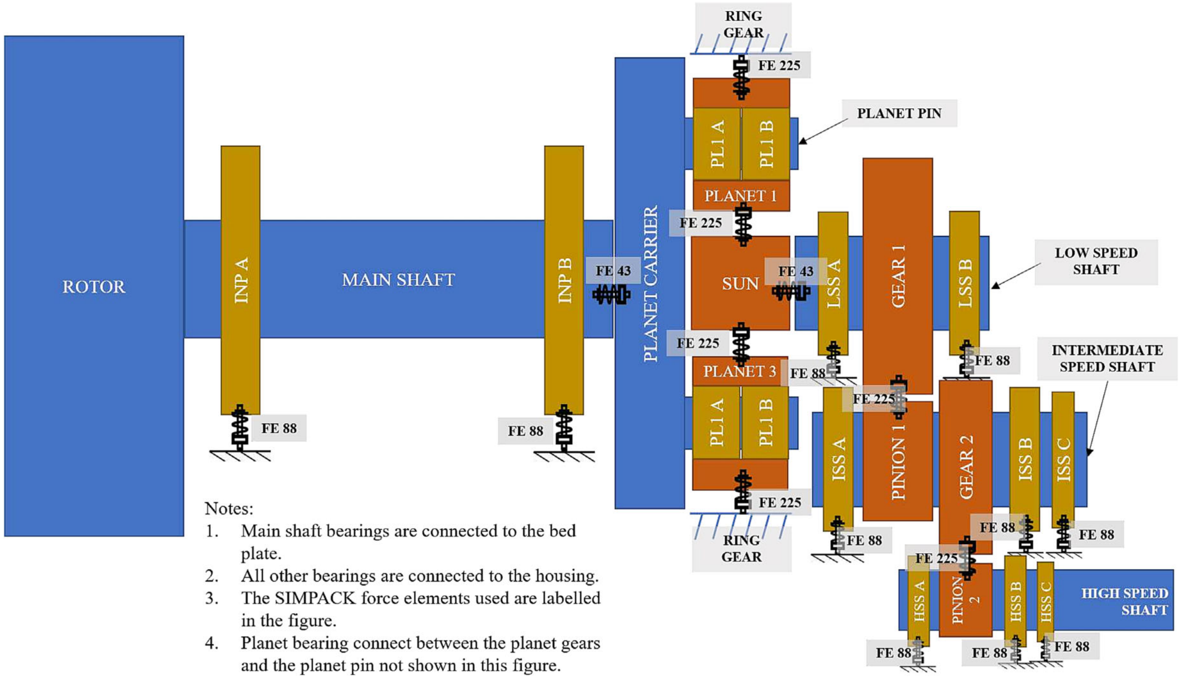

Notes:
1. Main shaft bearings are connected to the bed plate.
2. All other bearings are connected to the housing.
3. The SIMPACK force elements used are labelled in the figure.
4. Planet bearing connect between the planet gears and the planet pin not shown in this figure.

FIGURE 4 Schematic model of the drivetrain.

2.2 | 2MW DFIG

This subsection provides a brief description of the grid-connected DFIG and the associated rotor side and grid side control. The generator is modelled using the `Asynchronous Machine SI Units` block in Simulink®. The generator parameters are provided in Table A4. The stator is connected directly to the grid (the transformer is ignored), and the rotor is connected through the back-to-back AC/DC/AC converter. The grid is modelled using a `Three-Phase Programmable Voltage Source` Simulink® block, and the mechanical speed Ω_m of the shaft is obtained from the SIMPACK model and is assumed to be equal to the high-speed shaft velocity at the generator end. A majority of the blocks used to develop the grid-connected DFIG model are provided by the Simscape™ Electrical™ Specialized Power Systems library. The `powergui` is an environment block that contains the equivalent Simulink® circuit that represents the state-space equations of the models in the Simscape Electrical Specialized Power Systems library.

10991824, 0, Downloaded from https://onlinelibrary.wiley.com/doi/10.1002/we.2842 by Chalmers University Of Technology, Wiley Online Library on [19/06/2023]. See the Terms and Conditions (https://onlinelibrary.wiley.com/terms-and-conditions) on Wiley Online Library for rules of use; OA articles are governed by the applicable Creative Commons License

2.2.1 | Vector control of DFIG using an AC/DC/AC converter

The rotor side converter (RSC) and the grid side converter (GSC) controllers are modelled in the *dq* reference frame where the *d*-axis is aligned with the stator flux space vector. Due to this orientation, at the RSC, direct rotor current control is analogous to stator reactive power control, and quadrature rotor current control is analogous to stator active power control or electromagnetic torque control. At the GSC, direct grid current control is analogous to DC bus voltage control, and quadrature grid current control is analogous to grid reactive current control.

Control of RSC

The rotor side controller has a cascading structure with two control loops. The outer loop controls the stator's active and reactive power, and the inner loop controls the rotor's direct and quadrature currents. As noted previous, the *dq*-frame separates the two outputs, and hence, the torque/active power can be controlled independently using the *q* rotor current and the reactive power can be controlled independently by the *d* rotor current. In this paper, active and reactive power references are not used, thus eliminating the outer loops. Instead, during normal operation, i_{dr} (direct rotor current) is set to zero, minimizing reactive current, and *indirect speed control* method is used to set the reference electromagnetic torque based on the mechanical rotor speed. The reference and the measured rotor currents are then fed to two independent PI (proportional-integral) controllers to determine the reference rotor voltage. Finally, the reference rotor voltage is sent to the `PWM Generator (2-Level)` Simulink® block to generate switching signals for a two-level voltage source converter (VSC) modelled in Simulink® using an `Universal Bridge` block. The control architecture is shown in Figure 5B.

Control of GSC

The GSC controller is designed to control power flow through the rotor to the grid and the DC bus voltage of the back-to-back converter. The GSC controller also has a cascading structure similar to the RSC controller. Again, the *dq*-frame separates the control of the DC bus voltage and reactive power delivered to the grid. The DC bus voltage and the reactive power delivered at the grid can be controlled independently using the direct and quadrature grid currents, respectively. The DC bus voltage controller, typically a PI controller, is used to determine the reference grid direct current. The reactive power delivered at the grid can be set to zero, therefore rendering the reference quadrature grid current zero. However, the reactive grid power can be set to a reference value based on grid code requirements. The obtained reference signals and measured signals of the grid direct and quadrature currents are sent to two independent PI controllers to obtain the reference filter voltage. Similar to the RSC, the reference voltage signal is sent to a `PWM Generator (2-Level)` Simulink® block to generate switching commands for a two-level VSC. The control architecture is shown in Figure 5C.

2.2.2 | Performance during severe grid voltage dips

When a grid voltage dip is seen directly by the stator, the rotor voltage should simultaneously and significantly increase to prevent high rotor currents. However, due to the dimensioning of the converter, it can only provide the rotor with voltages of approximately one third of the stator voltage. Due to the slow evolution of stator flux and the rotor voltage limitation, the DFIG is unable to maintain rotor currents below the safe limits without losing control.[25] Crowbar protection is activated to accelerate flux evolution while simultaneously recovering converter control as quickly as possible to solve these problems imposed by the voltage dips.

As demanded by grid codes, to provide low voltage ride through (LVRT) capabilities, the wind turbine must remain connected during the voltage dip while providing reactive power through the stator. The step undertaken during a severe voltage dip in this paper is as follows:

1. Initially, the DFIG operates at a speed determined by inflow wind speed.
2. When the voltage dip occurs, it is detected by a rise in rotor current. However, this detection takes a few milliseconds (typically 0.5–5 ms), and the system cannot guarantee control during this period.
3. On detecting the voltage dip, the crowbar is activated to demagnetize the machine. While the crowbar is open, the converter is inhibited to protect it from overcurrent. The crowbar activation duration depends on the machine's design and is a compromise between safety and fulfilment of grid codes. Typically, the crowbar is activated for 50–200 ms.[26] In this paper, the crowbar is activated for 100 ms.
4. Once the flux has decayed, the crowbar is deactivated, and control is restored to the rotor converter. For the remaining duration of the fault, the entire rotor current is used to provide reactive power by setting *d*-current to the rated rotor current.
5. Once the voltage is recovered, normal operation is resumed.

10991824, 0, Downloaded from https://onlinelibrary.wiley.com/doi/10.1002/we.2842 by Chalmers University Of Technology, Wiley Online Library on [19/06/2023]. See the Terms and Conditions (https://onlinelibrary.wiley.com/terms-and-conditions) on Wiley Online Library for rules of use; OA articles are governed by the applicable Creative Commons License

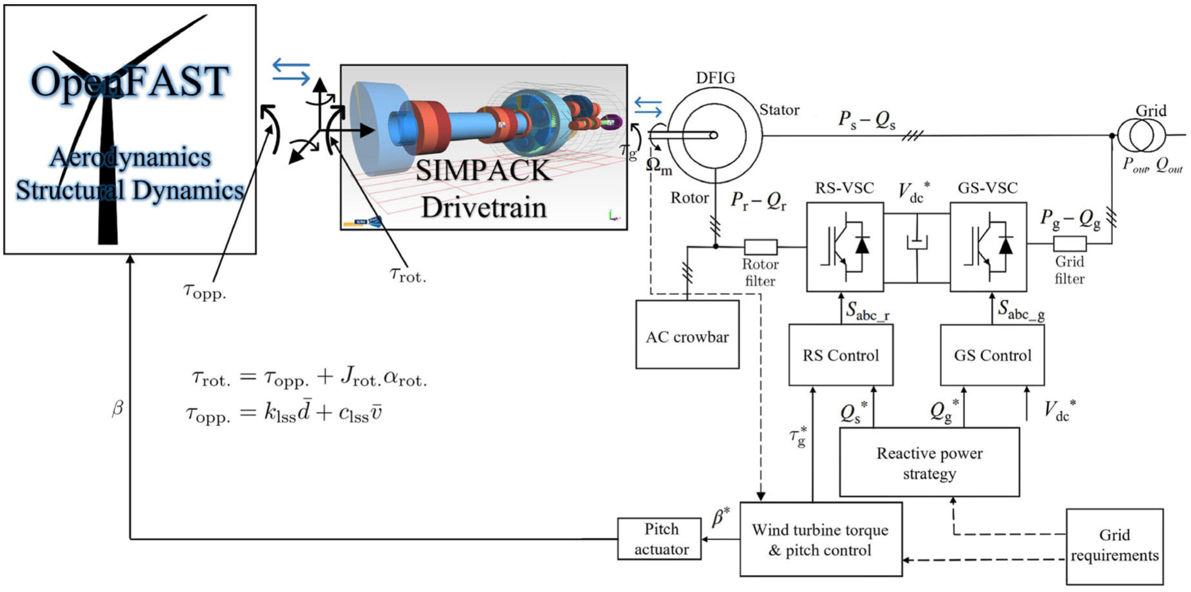

(A) Coupling OpenFAST, SIMPACK and DFIG

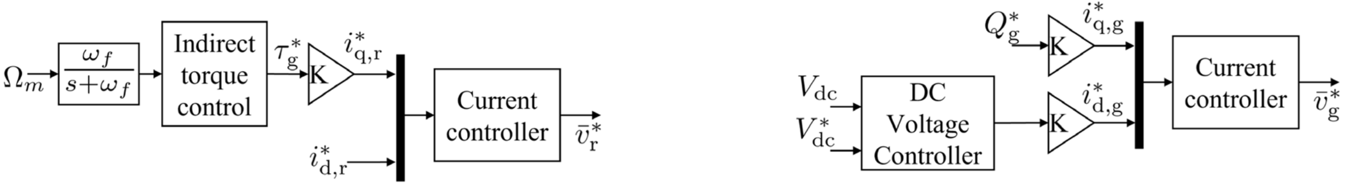

(B) Rotor side controller **(C)** Grid side controller

FIGURE 5 (A–C) Coupled OpenFAST, SIMPACK, DFIG and associated control systems.

2.3 | Coupling the drivetrain and generator models with OpenFAST

As described in the previous sections, the wind turbine is modelled in the open-source software OpenFAST,[27] the drivetrain is modelled in SIMPACK,[24] and the grid-connected DFIG is modelled in Simulink®. Therefore, the three models must be externally coupled. In this paper, the three models are coupled in Simulink®. OpenFAST offers an interface to Simulink® implemented as a `Level-2 S-Function` called `FAST S-Function`. The interface is written in C, and it calls a DLL of OpenFAST routines, which are written in FORTRAN. On the other hand, SIMPACK provides a co-simulation interface between SIMPACK and MATLAB® Simulink® called SIMAT. Using SIMAT, the two co-simulation partners exchange their results with a given time step using the TCP/IP protocol. This allows the user to take direct advantage of the complex mechanical systems modelled in SIMPACK and the control systems designed in Simulink®. The coupling mechanism adopted in this paper is motivated by the results presented in Girsang et al.[28] In this mechanism, the drivetrain torsional model in OpenFAST is turned off, and the gearbox ratio is set to 1. The resulting opposing torque is measured at the low-speed shaft and used in place of the opposing generator torque. The SIMPACK model, at the rotor end, accepts the three-dimensional rotor torques/moments and transverse forces. The force transfer is depicted graphically in Figure 5A. As mentioned in the previous section, the 2 MW DFIG model is developed in Simulink® and solved in discrete time using the `powergui` environment block. Zeroth-order hold is used in Simulink® to connect the continuous and discrete-time systems. The coupled system in Simulink® and the associated control systems are shown in Figure 5.

3 | MITIGATION OF TTRS

This section summarizes the three TTR mitigation methods investigated in this paper. In the first two subsections, the TMD and the asymmetric torque limiter are described. Next, a novel open-loop control strategy for the high-speed shaft mechanical break is presented.

10991824, 0, Downloaded from https://onlinelibrary.wiley.com/doi/10.1002/we.2842 by Chalmers University Of Technology, Wiley Online Library on [19/06/2023]. See the Terms and Conditions (https://onlinelibrary.wiley.com/terms-and-conditions) on Wiley Online Library for rules of use; OA articles are governed by the applicable Creative Commons License

3.1 | TMD

A TMD is installed in front of the generator and behind the high-speed shaft coupling of the wind turbine drivetrain as this presents the most convenient location on the generator side of the drivetrain. To design the torsional TMD, a simplified 2-degrees of freedom (DOF) model instead of the SIMPACK multibody model presented in Section 2.1 is used. Further, the generator and the torsional TMD are represented on the main shaft using the effective inertia and stiffness given in Equation A3. The schematic of the 2-DOF model coupled with the TMD is presented in Figure 6 resulting in a 3-DOF system where the degrees of freedom are $q=[q_{rot},q_{gen},q_d]$ represented on the main shaft of the drivetrain. All high-speed shaft parameters on the main shaft of the drivetrain are represented with the superscript ^{eff}.

For a chosen effective rotation inertia of the drivetrain, J_{TMD}^{eff} (or mass ratio of the TMD μ) the optimal effective stiffness k_{TMD}^{eff} (or tuning ratio β) and damping ratio ζ_d are estimated using the classical Den Hartog formula[29] as follows.

$$\beta=\frac{1}{1+\mu} \qquad \zeta_d=\sqrt{\frac{3\mu}{8(1+\mu)}} \tag{1}$$

The applicability of Den Hartog's formula in Equation (1) is described in Appendix A. The relationship between the inertia J_{TMD} and the spring stiffness k_{TMD} of the TMD on the high-speed shaft can also be obtained from Equation (A3). Typically, the TMD is tuned to the dominant eigenfrequency of the primary structure. The wind turbine drivetrain sketched in Figure 6 if modelled with a free-free boundary condition has an eigenfrequency given by Equation (A3). However, the drivetrain does not operate under a precise free-free boundary condition. Therefore, the dominant eigenfrequency is identified from numerical simulation as 1.53 Hz and is used to tune the TMD.

3.2 | Asymmetric torque limiter

The asymmetric torque limiter allows torque in one direction (locked clutch) while allowing free relative motion in the opposite direction (free clutch). With the asymmetric torque limiter connected between the high-speed shaft coupling and the generator shaft, the HSS coupling and the generator shaft can rotate in two directions. But the transmission of torque to the HSS coupling is limited only to one direction. This paper has used the SIMPACK force element `FE 19 One-Way Clutch Cmp` to model such an ideal asymmetric torque limiter. This force element is used to transmit torque in one direction (locked clutch) while allowing free relative motion in the opposite direction (free clutch). For example, an input shaft can rotate in two directions, but the transmission of torque to the output shaft is possible only in one direction. The transmission of torque is realized in only one direction of relative velocity between the input and the output shaft, depending on how the user sets the direction. The transmission starts or ends each time the direction of the relative velocity changes. In this paper, the `FE 19 One-Way Clutch Cmp` is locked when the joint velocity state is positive and unlocked (free) when the joint velocity state is negative. When the clutch is locked, it acts as a linear spring and damper to transmit the torque. Algorithmically, it can be expressed as follows:

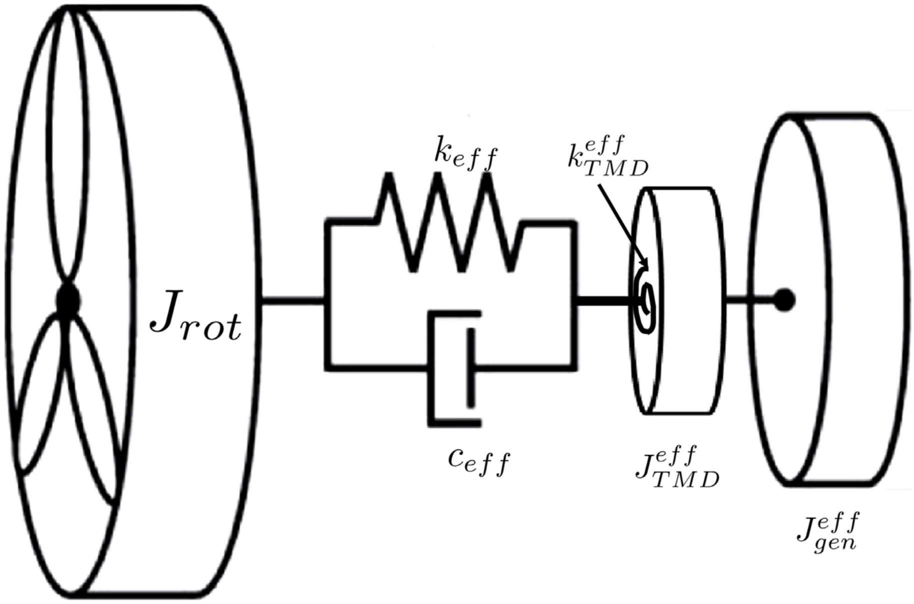

FIGURE 6 Schematic diagram of the drivetrain coupled with a torsional tuned mass damper (TMD).

10991824, 0, Downloaded from https://onlinelibrary.wiley.com/doi/10.1002/we.2842 by Chalmers University Of Technology, Wiley Online Library on [19/06/2023]. See the Terms and Conditions (https://onlinelibrary.wiley.com/terms-and-conditions) on Wiley Online Library for rules of use; OA articles are governed by the applicable Creative Commons License

```
if $q_c > \delta$ then
    $\tau = k_c q_c + c_c \dot{q}_c$
else
    $\tau = 0$
end if
```

where q_c is the relative rotation of the joint, k_c is the rotational stiffness and c_c is the rotational damping coefficient of the locked clutch. δ is the tolerance (a small negative quantity) and τ is the torque transmitted by the one-way clutch. To represent a locked clutch, the stiffness and damping must be chosen sufficiently high so as to not alter the drivetrain's natural frequencies. Parallelly, care must be taken to avoid numerical issues arising from very high stiffness. In this paper, the stiffness $k_c = 200 \times k_{HSS}$ and damping $c_c = 200 \times c_{HSS}$ are assumed.

3.3 | High-speed shaft brake

The fundamental reason for load-induced TTRs is the sudden change or absence of the generator torque at the generator end of the drivetrain. Therefore, it can be intuitively hypothesized that the fluctuations in the generator end of the drivetrain can be controlled actuation of the high-speed shaft brake which is mounted directly on the high-speed shaft. Based on this idea, an open-loop control strategy for the high-speed shaft brake is proposed in this paper with the aim to mitigate TTRs. The actuator of the friction disk brakes is modelled by a first-order system[30–32]

$$H(s) = \frac{\omega_0}{s + \omega_0} \tag{2}$$

where ω_0 is the bandwidth of the actuator. Literature[33] also suggests an actuator bandwidth of $\omega_0 = 72$ rad/s for brake with a torque rating similar to the one assumed in this paper. In this paper, first, an actuator bandwidth of 72 rad/s is assumed. Then, the effect of slower actuators on the performance of the disc brake is investigated by decreasing the bandwidth in Section 4.3.3.

Furthermore, the high-speed shaft brake torque capacity must be sufficiently large to deliver the torque required to mitigate the TTRs. According to DNVGL-ST-0437[34] and IEC 61400-1,[35] the most unfavourable load (maximum or minimum) for the mechanical brake can be obtained from DLC (Design Load Case) 8.1. The design torque for the high-speed shaft brake is obtained as

$$T_d = \gamma_f \gamma_m \gamma_n T_l \tag{3}$$

where $\gamma_f = 1.5$ is the partial safety factor for loads, $\gamma_m = 1.2$ is the partial safety factor for materials and $\gamma_n = 1.3$ and partial safety factor for consequences of failure. T_l is the aerodynamic moment obtained from the most unfavourable conditions corresponding to DLC 8.1. For the generic 2 MW wind turbine, the worst-case aerodynamic moment on the HSS is obtained as $T_l = 4.5$ kNm. Hence, the design braking torque is obtained as 10.5 kNm. The design braking torque is close to the rated generator torque of the turbine and is sufficient to mitigate TTRs as shown in the following sections. Furthermore, it can be noted that industrial disk brakes easily deliver these torque ratings.[36,37]

4 | RESULTS

In this subsection, the results are presented to demonstrate the capabilities of the three mitigation approaches described above. The section is divided into three subsections each of which is dedicated to each device/strategy. Two load cases (transient events) are considered here: (a) grid faults and (b) emergency shutdowns. The grid fault is represented by a symmetric voltage dip of 90%, and the detail of the sequence of events is provided in Table 1. In the emergency shutdown events, the wind turbine is simulated at different wind speeds, and the shutdown is initiated at 30 s. During the emergency shutdown, aerodynamic braking only is used whereby the blades are fully feathered to 90° with a maximum pitching rate.

In the following subsections, the performance of a TMD and an asymmetric torque limiter is demonstrated in Sections 4.1 and 4.2, respectively. Lastly, the TTR mitigation capabilities of the open-loop high-speed shaft brake are demonstrated in Section 4.3. It is important to point out that to demonstrate the capabilities and shortcomings of the TMD and the asymmetric torque limiter, first, the grid fault event is considered in Sections 4.1 and 4.2. The results and conclusion in case of the emergency shutdown events are provided later in Section 4.4.

10991824, 0, Downloaded from https://onlinelibrary.wiley.com/doi/10.1002/we.2842 by Chalmers University Of Technology, Wiley Online Library on [19/06/2023]. See the Terms and Conditions (https://onlinelibrary.wiley.com/terms-and-conditions) on Wiley Online Library for rules of use; OA articles are governed by the applicable Creative Commons License

4.1 | Simulation results for the TMD

The TMD is installed as described in Section 3.1 and tuned to the fundamental frequency of the drivetrain. The fundamental frequency of the drivetrain is obtained from numerical simulations. The inertia of the TMD is assumed to be 10% of the inertia of the generator rotor. The optimum linear stiffness and damping are estimated as per Equation (1).

The results are presented in Figure 7. In Figure 7, a 90% symmetric voltage dip is simulated at 10 s using the parameters presented in Table 1. It can be observed in Figure 7 that the torsional vibration characteristic of the drivetrain is improved by the installation of the TMD. The oscillations in the high-speed shaft torque and the radial bearing force initiated by the grid fault are mitigated to an appreciable extent by the TMD. However, it can be observed in Figure 7D that the BLRs are not mitigated by the TMD. Therefore, it can be concluded that the TMD improves the torsional characteristics of the drivetrain; however, it fails to mitigate the BLRs and the associated risk of slip including surface damage.

TABLE 1 Symmetrical voltage drop events.

Parameter	Value
Dip start	10 s
Crowbar open	10 s+1 ms
Crowbar close	10.1 s
Recovery start	10.5 s
Recovery end	11.1 s
Voltage drop	0.9 p.u
Recovery slope	15 p.μ/s

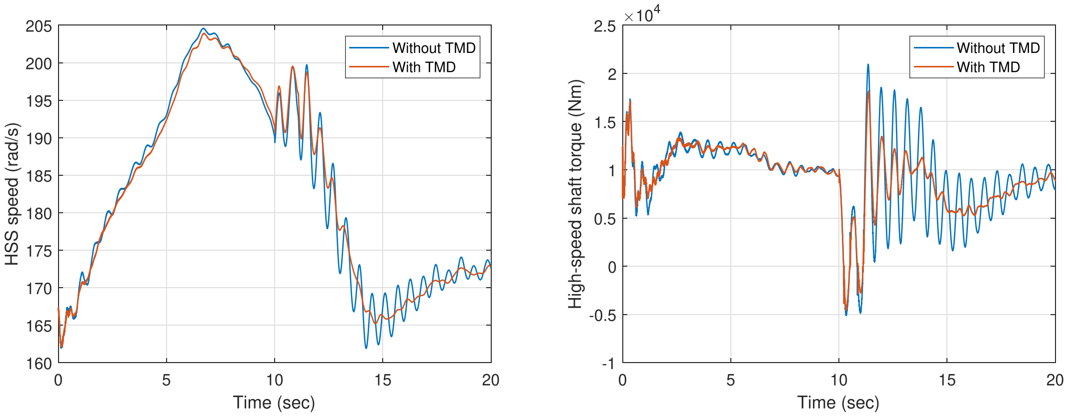

(A) High-speed shaft speed **(B)** High-speed shaft torque

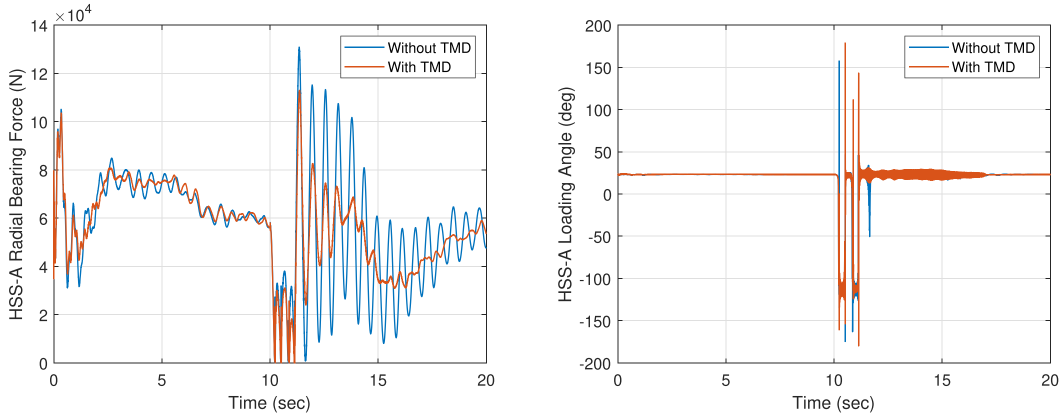

(C) High-speed shaft bearing A radial bearing force **(D)** High-speed shaft bearing A radial load angle

FIGURE 7 (A–D) High-speed shaft bearing A response at a wind speed of 12 m/s—with and without tuned mass damper. TMD, tuned mass damper.

10991824, 0, Downloaded from https://onlinelibrary.wiley.com/doi/10.1002/we.2842 by Chalmers University Of Technology, Wiley Online Library on [19/06/2023]. See the Terms and Conditions (https://onlinelibrary.wiley.com/terms-and-conditions) on Wiley Online Library for rules of use; OA articles are governed by the applicable Creative Commons License

4.2 | Simulation results for the asymmetric torque limiter

In this subsection, the performance of an asymmetric torque limiter is demonstrated. As described in Section 3.2, the results are presented in Figure 8, and it can be observed that the asymmetric torque limiter prevents the high-speed shaft torque from reversing its sign. In doing so, the asymmetric torque limiter improves the radial bearing loading characteristics in Figure 8C, but it is unable to prevent BLRs as shown in Figure 8D. Therefore, similar to the TMD, it can be concluded that while the asymmetric torque limiter can improve the torsional characteristics of the drivetrain, it fails to mitigate the BLRs and the associated risk of slip including surface damage.

4.3 | Simulation results for the high-speed shaft brake actuation

The novel proposal of active high-speed shaft brake actuation to mitigate TTRs is demonstrated in this subsection. The fundamental idea is to deploy the pre-existing mechanical brake during a transient event for a short duration to prevent TTRs. To demonstrate the capabilities of this method, both load cases are considered in the following including the symmetric voltage dip and emergency shutdown events.

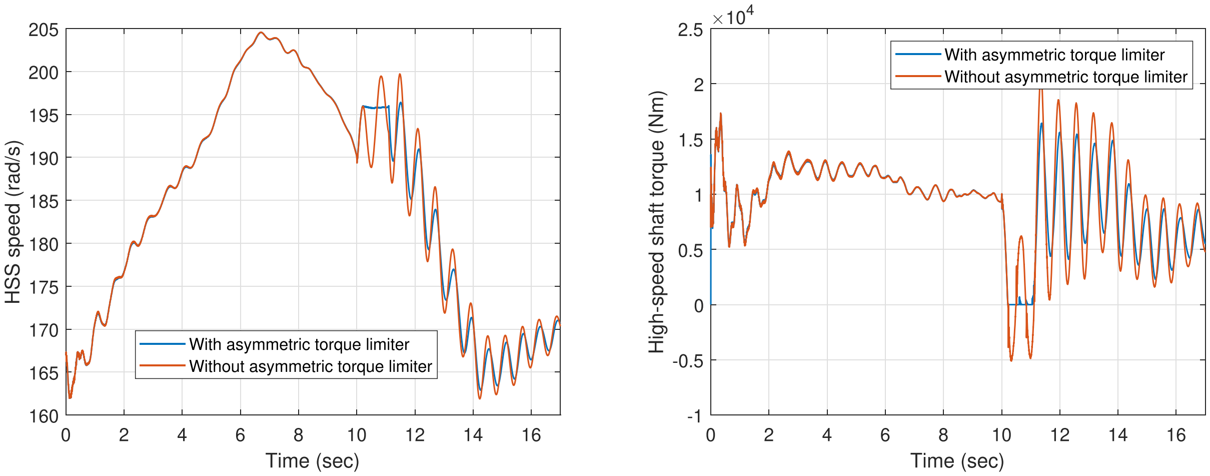

(A) High-speed shaft speed (B) High-speed shaft torque

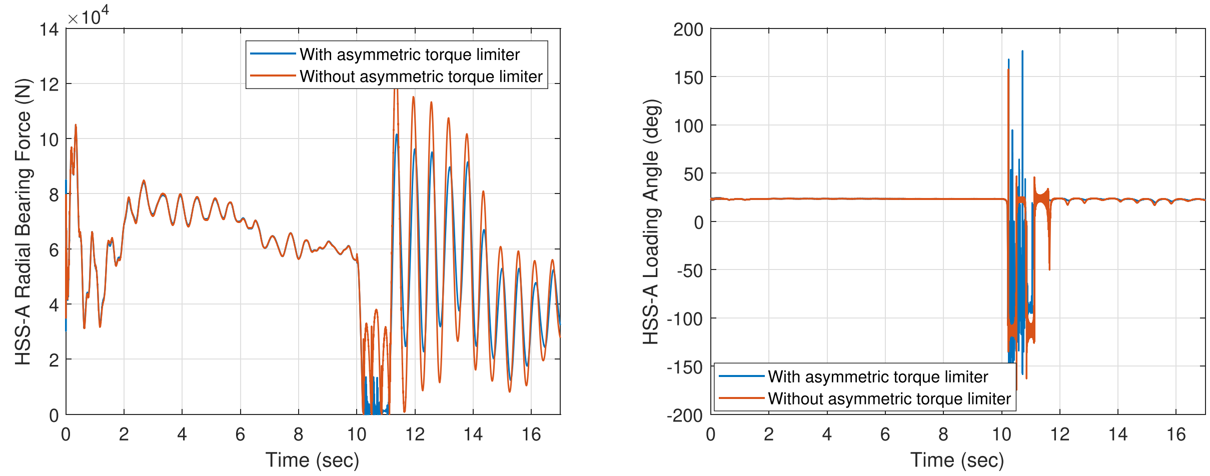

(C) High-speed shaft bearing A radial bearing force (D) High-speed shaft bearing A radial load angle

FIGURE 8 (A–D) High-speed shaft bearing A response at a wind speed of 12m/s—with and without asymmetric torque limiter. HSS, high-speed shaft.

10991824, 0, Downloaded from https://onlinelibrary.wiley.com/doi/10.1002/we.2842 by Chalmers University Of Technology, Wiley Online Library on [19/06/2023]. See the Terms and Conditions (https://onlinelibrary.wiley.com/terms-and-conditions) on Wiley Online Library for rules of use; OA articles are governed by the applicable Creative Commons License

4.3.1 | Symmetric voltage dip

The open-loop control for the mechanical brake has three fundamental parameters: (a) the brake torque magnitude, (b) the brake duration and (c) the bandwidth of the torque actuator. In this subsection, first, the effect of the brake torque magnitude and the brake duration is investigated. Using the *slip-risk duration* metric introduced in Section 1, the risk of damage associated with an event can be quantified. Graphically, the slip-risk duration can be represented as the summation of the shaded areas in Figure 9. Note the difference in the time scale in Figure 9A,B. It can be observed that the slip-risk duration during a grid fault event at low wind speeds is much higher than the same event at a higher wind speed, and the transient response of the bearing is very different. It can also be noted that in these two events, the mechanical HSS brake is unable to mitigate the TTRs.

Next, the effect of the brake torque magnitude and the brake duration on the *slip-risk duration* is evaluated through a sensitivity analysis and is presented in Figure 10. Figure 10 shows the contour plots of the *slip-risk duration*. In the contour plot, the third parameter is held at the baseline value shown in the title of the plot. The important results obtained from the sensitivity study are enumerated in the following.

First, some high-level commentary is made as follows:

1. The slip-risk duration generally reduces with increasing wind speeds/rotor torque, brake torque magnitude and braking duration. We consider that for a *slip-risk duration* below 50 ms, the slip risk is mitigated for all practical purposes.
2. Considering the entire domain of operation, the results show that the slip risk can be eliminated by applying the HSS brake with a magnitude of 40%–50% of the rated generator torque for a duration of > 1 s.

Next, some finer observations are made as follows:

1. In Figure 10, the first contour plot shows the contours of the slip-risk duration with respect to HSS torque and brake torque (in terms of percentage of rated generated torque). Generally, the slip-risk duration decreases with increasing HSS torque and brake torque. However, a valley can be observed that shows that the slip-risk duration is lower at the braking torque of 30% compared with 15% or 45%. These three points are marked on the plot with diamond markers. To elaborate on these three cases, the time histories of these events are plotted in Figure 11. It can be observed that the dynamic characteristics of the radial bearing load at a brake torque of 30% are better compared with 15% or 45%.
2. In Figure 10, the third plot shows a valley where the *slip-risk duration* is lower at a brake duration of 0.55 s compared with 0.25 s or 0.85 s. These three points are marked on the plot with diamond markers. To elaborate on these three cases, the time histories of these events are plotted in Figure 12. Here again, the dynamic characteristics of the bearing load at a brake duration of 0.55 s are better compared with 0.25 s or 0.85 s.

These observations elucidate two important ideas:

1. The brake torque magnitude and brake duration are strongly coupled to the fault in terms of the voltage dip level, the recovery speed, the duration of the fault and so on. Therefore, for each event, there exists an ‘optimum’ that can mitigate the TTRs with minimum effort.

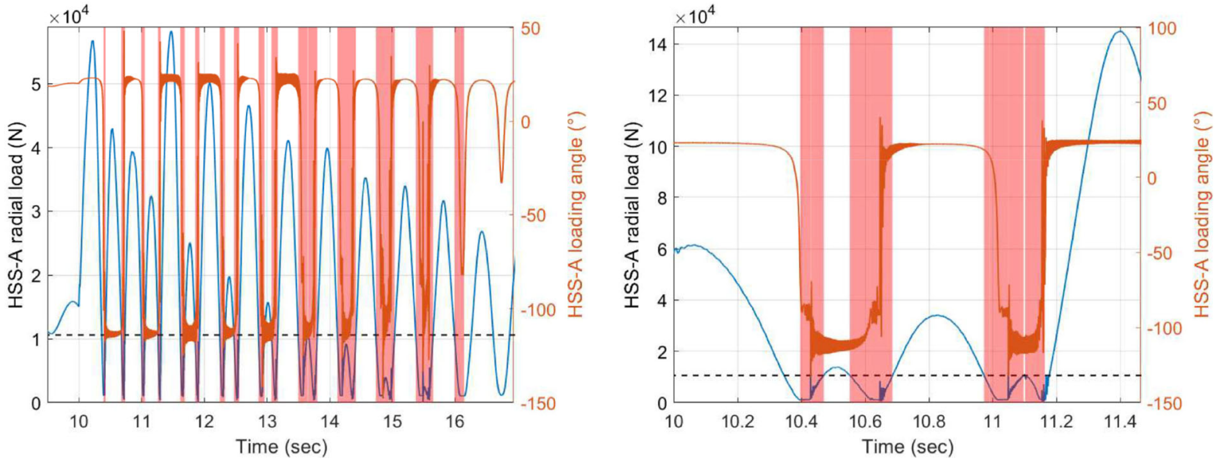

(A) Wind speed 6m/s **(B)** Wind speed 9m/s

FIGURE 9 (A, B) Shaded area showing the slip-risk duration for different wind speeds for a brake torque of 45% and a brake duration of 250 ms (note the difference in *x*-axis scale in the two figures). HSS, high-speed shaft.

10991824, 0, Downloaded from https://onlinelibrary.wiley.com/doi/10.1002/we.2842 by Chalmers University Of Technology, Wiley Online Library on [19/06/2023]. See the Terms and Conditions (https://onlinelibrary.wiley.com/terms-and-conditions) on Wiley Online Library for rules of use; OA articles are governed by the applicable Creative Commons License

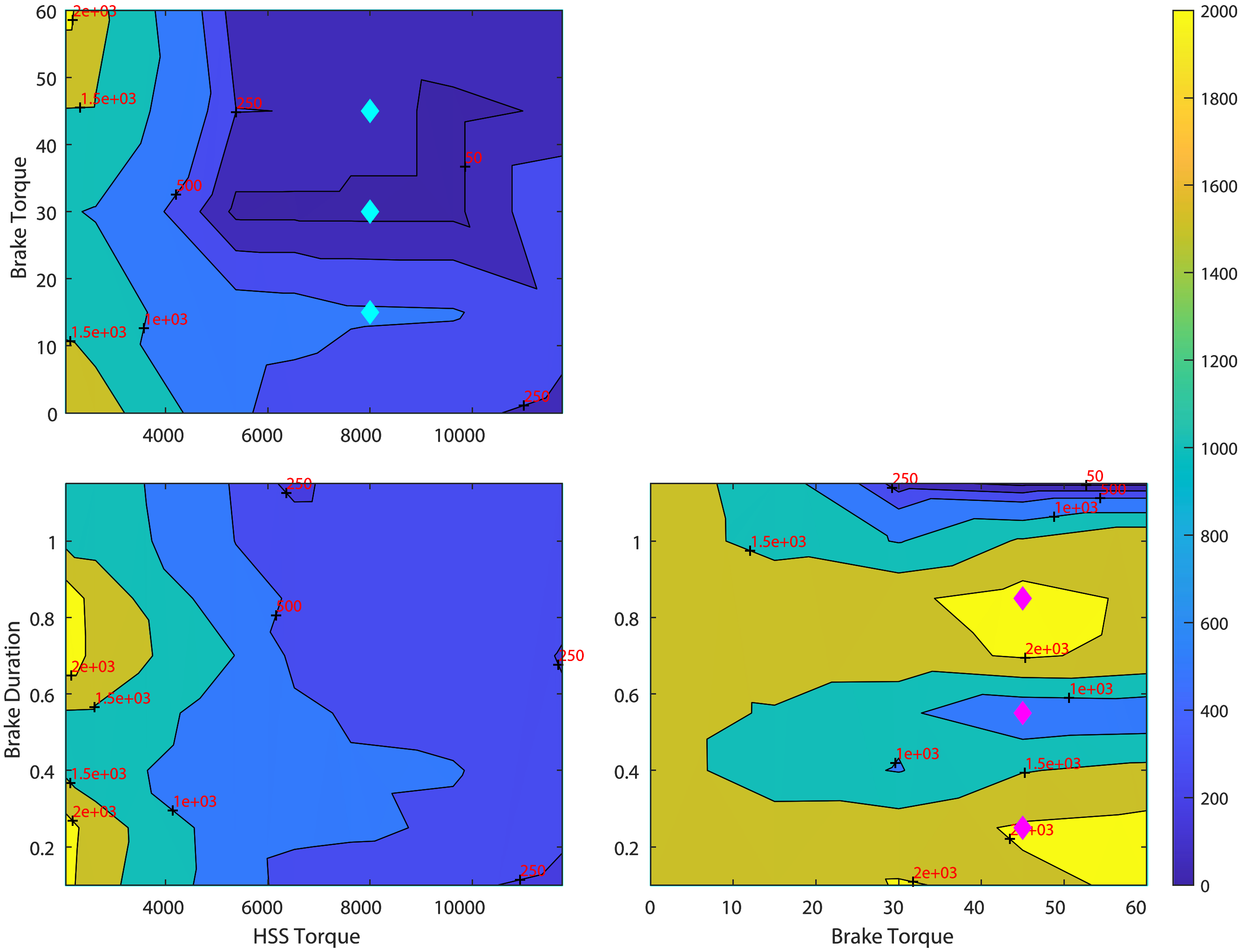

FIGURE 10 Contour plots of *slip-risk duration* with respect to high-speed shaft (HSS) torque (in Nm), braking torque (in % of rated generator torque) and brake duration (in seconds)

2. This ‘optimum’ brake torque and brake duration is dependent on the fault characteristics, and each fault type requires separate consideration. One way of approaching this problem is with closed-loop control architecture. But, in this paper, for the purposes of proof-of-concept and ease of construction, an open-loop controller is adopted. In the open-loop control architecture, the brake torque magnitude and brake duration are selected to mitigate all cases of grid faults.

The results show that drivetrain (bearing) dynamics and the associated slip-risk duration are heavily coupled to the transience created by braking parameters. The analyses show that the slip risk is significantly reduced if the right parameters (in terms of brake torque magnitude and brake duration) are selected to land in the valleys of the contour plots. However, not only is finding these parameters difficult but they are also extremely sensitive to the dynamics of the drivetrain and the wind turbine. Therefore, the more intuitive and conservative design suggests selecting the braking parameters such as the slip-risk duration is eliminated for all operating conditions. Figure 10 shows that slip risk can be eliminated by applying the HSS brake with a magnitude of 40%–50% of the rated generator torque for a duration of > 1 s.

It can be observed here that the required brake duration is closely connected to the duration of the fault. Grid codes suggest that the turbine should resume operation when the fault is recovered to 90% of the prefault level. With that in regard, further investigation has been carried out, and it was found that the TTRs can be mitigated by ceasing the braking action when the fault is recovered to 90% of the prefault event (results omitted for brevity). Therefore, it is recommended in this paper, that for symmetric voltage dips, the mechanical brake be deployed when the rotor crowbar is activated using the same trigger. The braking magnitude must be 50% of the rated generator torque. The braking is stopped when the fault is recovered to 90% of the prefault level when the turbine is required to resume normal operation.

10991824, 0, Downloaded from https://onlinelibrary.wiley.com/doi/10.1002/we.2842 by Chalmers University Of Technology, Wiley Online Library on [19/06/2023]. See the Terms and Conditions (https://onlinelibrary.wiley.com/terms-and-conditions) on Wiley Online Library for rules of use; OA articles are governed by the applicable Creative Commons License

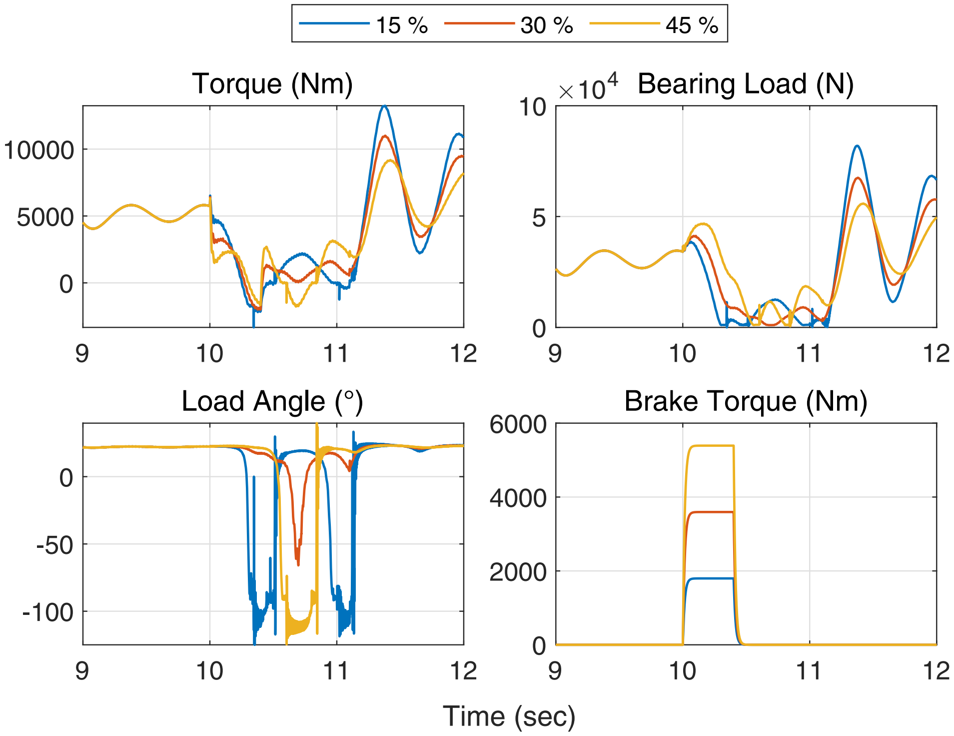

FIGURE 11 Effect of varying braking torque magnitude on high-speed shaft bearing dynamics during fault.

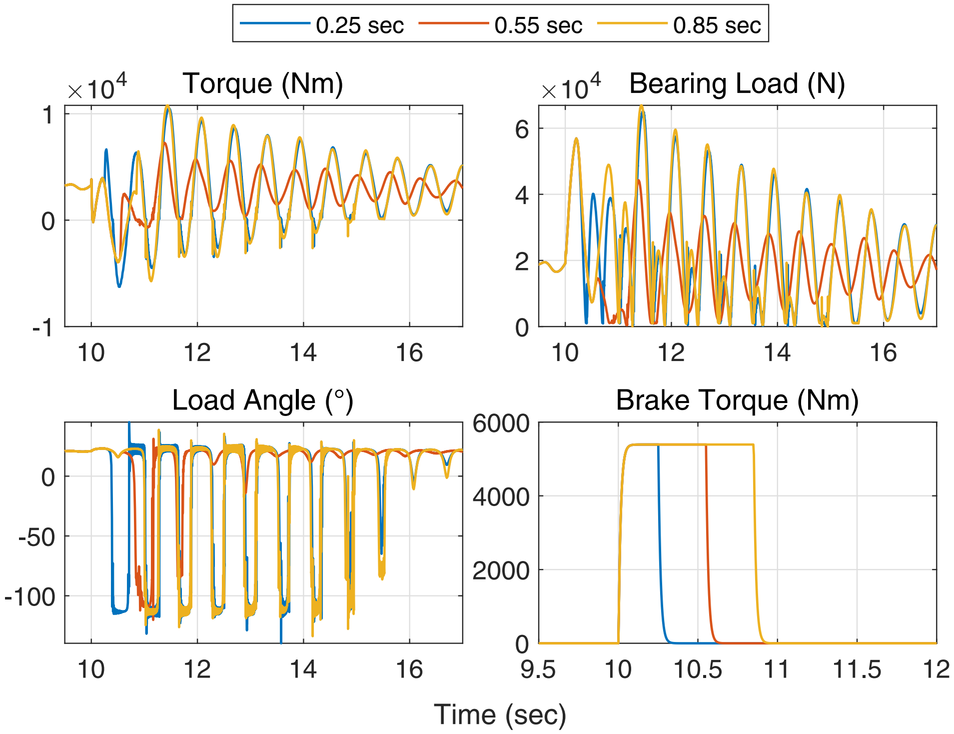

FIGURE 12 Effect of varying braking duration on high-speed shaft bearing dynamics during fault.

10991824, 0, Downloaded from https://onlinelibrary.wiley.com/doi/10.1002/we.2842 by Chalmers University Of Technology, Wiley Online Library on [19/06/2023]. See the Terms and Conditions (https://onlinelibrary.wiley.com/terms-and-conditions) on Wiley Online Library for rules of use; OA articles are governed by the applicable Creative Commons License

4.3.2 | Emergency shutdown

In this subsection, the mechanical HSS brake is used to mitigate TTRs during emergency shutdown events. During emergency shutdown events, the brake is deployed at the same time when the emergency shutdown is initiated and the braking is stopped when the high-speed shaft speed is lower than 50 rpm. The magnitude of the braking torque is determined by a sensitivity analysis. Figure 13 shows that a braking torque of 80% of the rated generator torque is required to mitigate TTRs at a wind speed of 26 m/s. It can also be noted here that it was found that a braking torque of 60% was required at a wind speed of 12 m/s to mitigate the slip risk. Therefore, for a conservative design, a braking torque magnitude of 80% of the rated generator torque is recommended in this paper for all emergency shutdown events. It can be noted here that 80% of the rated generator torque amounts to 9.6 kNm which is lower than the design braking torque of the mechanical brake estimated in Section 3.3.

4.3.3 | High-speed shaft brake actuator bandwidth and dead time

The performance of the high-speed shaft mechanical brake depends on the actuator dynamics. The pneumatic actuator of the mechanical brake can be approximately modelled by a first-order system as described in Section 3.3. In a first-order system, the bandwidth and the dead time dictate the response of the actuator to the control demand.

The effect of the actuator bandwidth and the dead time on the performance of the mechanical brake are investigated and demonstrated in Figures 14 and 15, respectively. Figure 14 shows that the actuator offers significant mitigation capabilities with bandwidths as low as 18 rad/s which is significantly lower than the generally accepted actuator bandwidths for brake of similar torque rating.[33] The performance starts to deteriorate significantly at lower bandwidths of 9 rad/s and below.

Figure 15 shows that the performance of the brake deteriorates significantly when the initial dead time is greater than or equal to 250 ms. However, up to 100 ms the brake offers excellent TTRs mitigation capabilities.

4.4 | Comparison of TTR mitigation strategies

In this subsection, the mitigation strategies investigated in this paper are compared. For qualitative comparison purposes, the mechanical damper termed reverse torsional damping (RTD) proposed in Eatherton et al[15] has also been included in the comparison. Furthermore, as the results in[15]

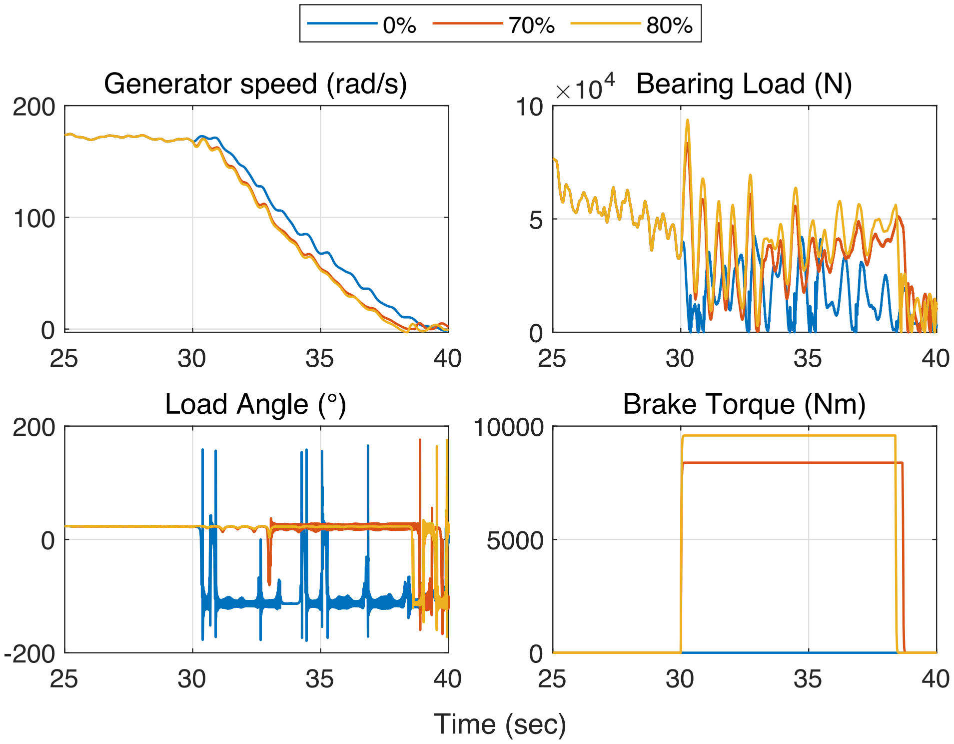

FIGURE 13 Emergency shutdown at 26 m/s.

10991824, 0, Downloaded from https://onlinelibrary.wiley.com/doi/10.1002/we.2842 by Chalmers University Of Technology, Wiley Online Library on [19/06/2023]. See the Terms and Conditions (https://onlinelibrary.wiley.com/terms-and-conditions) on Wiley Online Library for rules of use; OA articles are governed by the applicable Creative Commons License

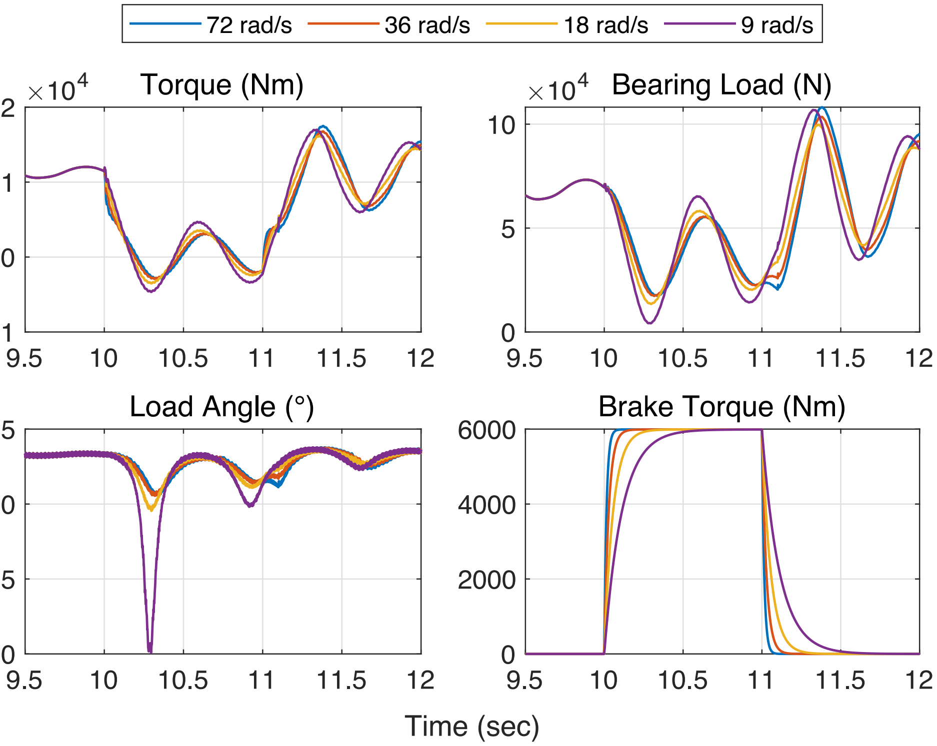

FIGURE 14 Effect of actuator bandwidth.

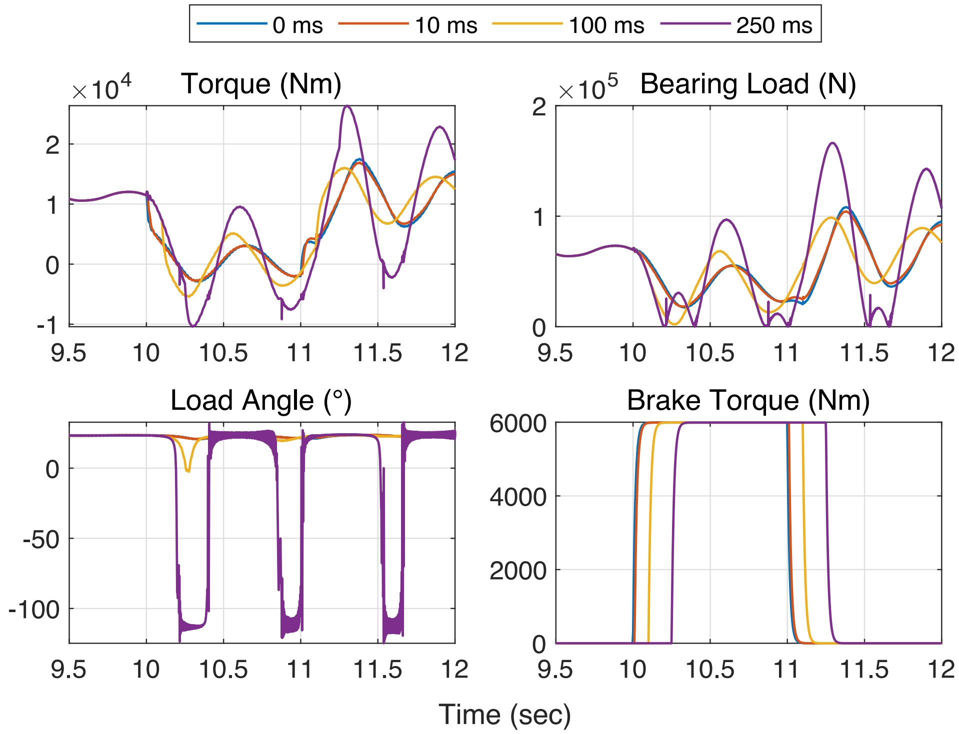

FIGURE 15 Effect of initial dead time.

are obtained from field measurements, it gives an opportunity to compare the results presented in this paper against measurements from operational wind turbines. However, it is important to note that the RTD investigated by Eatherton et al[15] has not been modelled in this paper. Furthermore, the turbine considered by Eatherton et al[15] is a 1.65 MW machine, and the environmental loading the turbine is subjected to during the measurement cannot be replicated here. An emergency shutdown case with aerodynamic braking only is considered for comparison. The results

10991824, 0, Downloaded from https://onlinelibrary.wiley.com/doi/10.1002/we.2842 by Chalmers University Of Technology, Wiley Online Library on [19/06/2023]. See the Terms and Conditions (https://onlinelibrary.wiley.com/terms-and-conditions) on Wiley Online Library for rules of use; OA articles are governed by the applicable Creative Commons License

obtained from this study are compared against Figures 4 and 5 in Eatherton et al.[15] To compare the different devices, three parameters are chosen as follows:

- Peak-to-peak HSS torque—the maximum peak-to-peak amplitude after the emergency shutdown has been initiated.
- Maximum negative HSS torque excursion—maximum negative torque recorded in the high-speed shaft after the emergency shutdown has been initiated.

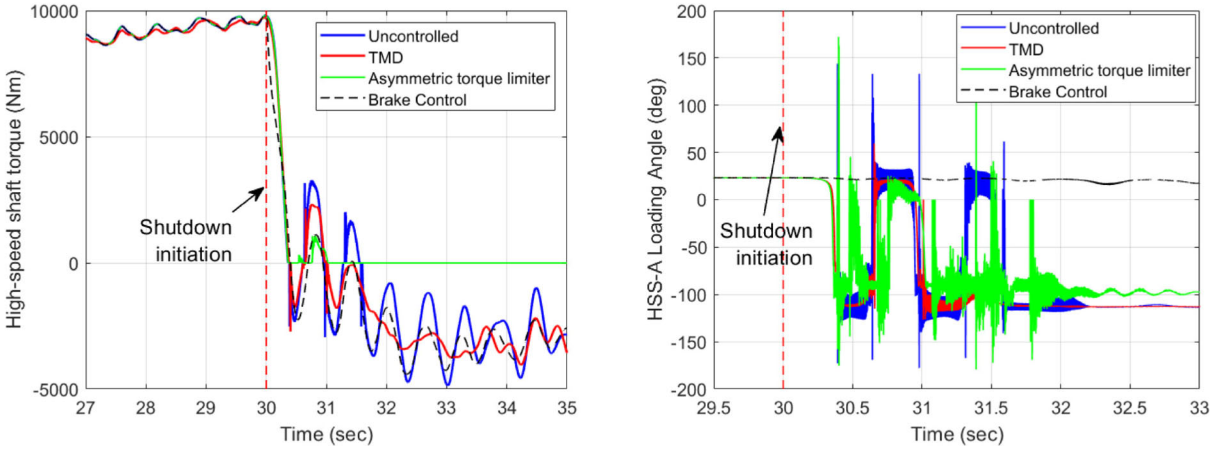

(A) HSS torque **(B)** Bearing load angle

FIGURE 16 (A, B) Comparison of mitigation methods—emergency shutdown. HSS, high-speed shaft; TMD, tuned mass damper.

TABLE 2 Ratio of controlled response to the uncontrolled/baseline response—emergency shutdown.

Response parameters	Tuned mass damper	Asymmetric torque limiter	RTD reported by Eatherton et al.[15][a]	Proposed brake control
Peak-to-peak HSS torque	0.65	0.18	0.50	0.55
Maximum negative HSS torque excursion	0.83	0.00	0.53	0.89
Slip-risk duration	0.83	2.74	–	0.00

[a] This is a representative comparison. The RTD proposed by Eatherton et al,[15] the turbine and the environment loading have not been replicated in this paper.

Abbreviations: HSS, high-speed shaft; RTD, reverse torsional damping.

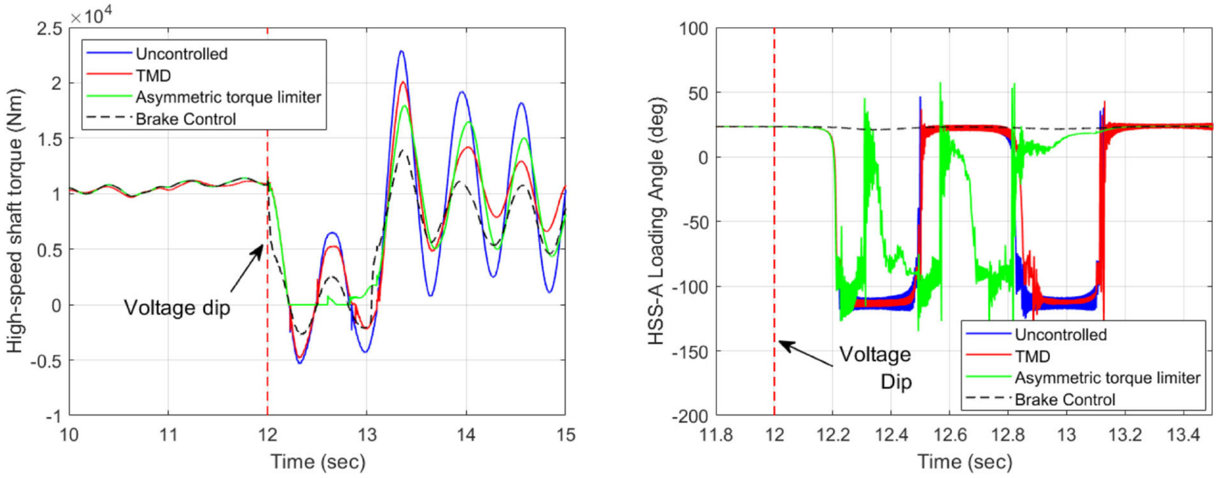

(A) HSS torque **(B)** Bearing load angle

FIGURE 17 Comparison of mitigation methods—symmetrical voltage dip. HSS, high-speed shaft.

10991824, 0, Downloaded from https://onlinelibrary.wiley.com/doi/10.1002/we.2842 by Chalmers University Of Technology, Wiley Online Library on [19/06/2023]. See the Terms and Conditions (https://onlinelibrary.wiley.com/terms-and-conditions) on Wiley Online Library for rules of use; OA articles are governed by the applicable Creative Commons License

TABLE 3 Ratio of controlled response to the uncontrolled/baseline response—symmetrical voltage dip.

Response parameters	Tuned mass damper	Asymmetric torque limiter	Proposed brake control
Peak-to-peak HSS torque	0.69	0.57	0.38
Maximum negative HSS torque excursion	0.90	0.00	0.50
Slip-risk duration	1.62	2.86	0.00

Abbreviation: HSS, high-speed shaft.

- Slip-risk duration—the metric proposed in this paper that estimates the time spent by the bearings in high slip risk. This metric cannot/has not been evaluated for the RTD proposed in Eatherton et al.[15]

The results are compared against the uncontrolled case and graphically presented in Figure 16 and quantitatively (in terms of the ratio to the uncontrolled case) in Table 2. The results show that while the TMD and the asymmetric torque limiter are capable of reducing peak-to-peak HSS torque amplitude and the negative HSS torque excursion, they are unable to reduce the *slip-risk duration*. In fact, the asymmetric torque limiter seems to increase the *slip-risk duration* thus deteriorating the bearing loading characteristics. The RTD proposed by Eatherton et al[15] reduces the peak-to-peak oscillation amplitude and the maximum negative torque excursion. However, its effect on the *slip-risk duration* cannot be determined. Finally, the proposed brake control strategy is capable of fully mitigating the *slip-risk duration* while simultaneously reducing the peak-to-peak oscillation amplitude and the maximum negative torque excursion.

To conclude, a similar comparison is carried out for the symmetrical voltage drop event in Figure 17. The results (in terms of the ratio to the uncontrolled case) are provided in Table 3. In this case, the RTD proposed in Eatherton et al[15] is eliminated from the comparison as the model is not available. Again, it can be observed that the TMD and the asymmetric torque limited can improve the HSS torque characteristics in terms of peak-to-peak amplitude and maximum negative excursion, but they are unable to mitigate the *slip risk*. On the other hand, the proposed brake control is capable of mitigating the *slip risk* in addition to the peak-to-peak amplitude and the maximum negative incursion.

5 | CONCLUSIONS

This paper investigated three methods of mitigating TTRs in an indirect drive DFIG wind turbine drivetrain. In this regard, first, two existing devices in the industry, namely, the TMD and the asymmetric torque limiter, were investigated. To investigate the performance of these methods, a high-fidelity model is developed by coupling together a wind turbine model in OpenFAST, a drivetrain model in SIMPACK and a grid-connected DIFG model in Simulink. The developed model allows the investigation of the coupled electromechanical dynamics of the wind turbine. Within the framework of the developed numerical models, it was shown that while these devices are capable of improving the torsional characteristics of the drivetrain in terms of peak-to-peak amplitude and maximum negative torque excursion in the high-speed shaft, they are unable to mitigate the *slip risk* associated to the transient events of symmetric voltage dips and emergency shutdowns investigated in this paper. To successfully mitigate the *slip risk* associated with TTRs, a novel approach of using the pre-existing high-speed shaft mechanical brake in an open-loop architecture has been proposed. The results presented in this paper show that the proposed brake control is capable of mitigating the *slip risk* associated with TTRs in the drivetrain. The paper has also shown that the mechanical brake is capable of mitigating the *slip risk* with the mechanical limitations in terms of torque rating, actuator bandwidth and initial dead time in place. For the two transient events considered in this paper, the following recommendations are offered:

- **Symmetric voltage drops**: The mechanical brake is deployed together with the electrical crowbar that protects the rotor against overcurrent using the same electronic trigger. The brake is deployed to achieve a torque of 50% of the rated generator torque. It is turned off when the voltage recovers to 90% of its prefault level.
- **Emergency shutdown events**: The mechanical brake is deployed when the emergency shutdown is initiated using the same trigger. The brake is deployed to achieve a torque of 80% of the rated generator torque. It is turned off when the generator speed is below 50 rpm.

The authors want to highlight that further research is required to identify other types of events (grid, converter and generator faults) that may lead to TTRs and increase the risk of slip-induced surface damage in gearbox bearings.

List of symbols used in this paper is as follows:

LIST OF SYMBOLS

$\tau_{opp.}$	Opposing torque measured at the rotor end of the main shaft
$\tau_{rot.}$	Rotor aerodynamic torque

10991824, 0, Downloaded from https://onlinelibrary.wiley.com/doi/10.1002/we.2842 by Chalmers University Of Technology, Wiley Online Library on [19/06/2023]. See the Terms and Conditions (https://onlinelibrary.wiley.com/terms-and-conditions) on Wiley Online Library for rules of use; OA articles are governed by the applicable Creative Commons License

τ_g	Generator electromagnetic torque
$J_{rot.}$	Rotor rotational inertia
$\alpha_{rot.}$	Rotor angular acceleration
k_{ms}	Elastic stiffness of main shaft
c_{lss}	Damping coefficient of the main shaft
$\overline{d}$	Relative displacement of the main shaft ends
$\overline{v}$	Relative velocity of the main shaft ends
P_s	Stator active power
Q_s	Stator reactive power
P_r	Rotor active power
Q_r	Rotor reactive power
P_g	Grid active power
Q_g	Grid reactive power
P_{out}	Output active power
Q_{out}	Output reactive power
V_{dc}	DC bus voltage
β	Wind turbine blade pitch angle
Ω_{m}	High-speed shaft or generator rotational speed
d	Bearing bore diameter
D	Bearing outer diameter
B	Bearing width
C_1	Bearing basic dynamic load rating
C_0	Bearing basic static load rating
ω_f	Filter cut-off frequency
$i^*_{\mathrm{q,r}}$	Reference rotor quadrature current
$i^*_{\mathrm{d,r}}$	Reference rotor direct current
$i^*_{\mathrm{q,g}}$	Reference grid quadrature current
$i^*_{\mathrm{d,g}}$	Reference grid direct current
$\overline{v}^*_{\mathrm{r}}$	Reference rotor voltage
$\overline{v}^*_{\mathrm{g}}$	Reference grid voltage
Ω	Rated rotor speed of the wind turbine
q_{rot}	Rotational state of the wind turbine rotor
q_{gen}	Rotational state of the wind turbine generator
q_d	Rotational state of the torsional tuned mass damper
J_{TMD}	Rotational inertia of the torsional tuned mass damper
k_{TMD}	Rotational stiffness of the torsional tuned mass damper
c_{TMD}	Rotational damping coefficient of the torsional tuned mass damper
N_1	Gear ratio of the planetary stage
N_2	Gear ratio of the first parallel stage
N_3	Gear ratio of the second parallel stage
N	Gear ratio of the gearbox
μ	Mass ratio of the torsional tuned mass damper
ζ_d	Damping ratio of the torsional tuned mass damper
ω_r	Tuning ratio of the torsional tuned mass damper
J_{rot}	Rotational inertia of the wind turbine rotor
J^{eff}_{gen}	Effective rotational inertia of the wind turbine rotor
k_{MS}	Rotational stiffness of the main shaft
k_{LSS}	Rotational stiffness of the low-speed shaft
k_{ISS}	Rotational stiffness of the intermediate speed shaft
k_{HSS}	Rotational stiffness of the high-speed shaft
J_{PC}	Rotational inertia of the planet carrier
J_S	Rotational inertia of the sun gear
J_{G1}	Rotational inertia of gear 1

10991824, 0, Downloaded from https://onlinelibrary.wiley.com/doi/10.1002/we.2842 by Chalmers University Of Technology, Wiley Online Library on [19/06/2023]. See the Terms and Conditions (https://onlinelibrary.wiley.com/terms-and-conditions) on Wiley Online Library for rules of use; OA articles are governed by the applicable Creative Commons License

J_{G2}	Rotational inertia of gear 2
J_{G3}	Rotational inertia of gear 3
J_{gen}	Rotational inertia of the wind turbine generator
k_c	Rotational stiffness of the asymmetric torque limiter in locked state
c_c	Rotational damping coefficient of the asymmetric torque limiter in locked state
ω_0	Bandwidth of the brake actuator first-order system

ACKNOWLEDGEMENTS

This project is financed through the Swedish Wind Power Technology Centre (SWPTC). SWPTC is a research centre for the design of wind turbines. The purpose of the centre is to support the Swedish industry with knowledge of design techniques as well as maintenance in the field of wind power. The centre is funded by the Swedish Energy Agency, Chalmers University of Technology, as well as academic and industrial partners.

DATA AVAILABILITY STATEMENT

The data that support the findings of this study are available from the corresponding author upon reasonable request.

ORCID

Saptarshi Sarkar https://orcid.org/0000-0002-2111-2154
Viktor Berbyuk https://orcid.org/0000-0002-8862-1148

PEER REVIEW

The peer review history for this article is available at https://www.webofscience.com/api/gateway/wos/peer-review/10.1002/we.2842.

REFERENCES

1. Council GWE. GWEC global wind report 2022. In: Global Wind Energy Council; 2022.
2. Fortune Business Insights. Wind turbine gearbox market size, share | growth, 2021-2028. 2022. Accessed March 20, 2023. https://www.fortunebusinessinsights.com/industry-reports/wind-turbine-gearbox-market-101355
3. van de Kaa G, van Ek M, Kamp LM, Rezaei J. Wind turbine technology battles: gearbox versus direct drive-opening up the black box of technology characteristics. *Technol Forecast Social Change*. 2020;153:119933.
4. Dao C, Kazemtabrizi B, Crabtree C. Wind turbine reliability data review and impacts on levelised cost of energy. *Wind Energy*. 2019;22(12):1848-1871.
5. Artigao E, Martín-Martínez S, Honrubia-Escribano A, Gómez-Lázaro E. Wind turbine reliability: a comprehensive review towards effective condition monitoring development. *Appl Energy*. 2018;228:1569-1583.
6. Sheng S. Report on wind turbine subsystem reliability—a survey of various databases (presentation). tech. rep., Golden, CO (United States), National Renewable Energy Lab.(NREL); 2013.
7. Musial W, Butterfield S, McNiff B. Improving wind turbine gearbox reliability. tech. rep., Golden, CO (United States), National Renewable Energy Lab.(NREL); 2007.
8. Evans RD, Barr TA, Houpert L, Boyd SV. Prevention of smearing damage in cylindrical roller bearings. *Tribology Trans*. 2013;56(5):703-716.
9. Evans M-H. An updated review: white etching cracks (WECS) and axial cracks in wind turbine gearbox bearings. *Materials Sci Technol*. 2016;32(11):1133-1169.
10. Stadler K, Lai J, Vegter R. A review: the dilemma with premature white etching crack (WEC) bearing failures. *Bearing Steel Technol: 10th Vol Adv Steel Technol Rolling Bearings*. 2015;1-22.
11. Sharpley N. Understanding the root causes of axial cracking in wind turbine gearbox bearings. 2014. https://www.windpowerengineering.com/understanding-root-causes-axial-cracking-wind-turbine-gearbox-bearings/
12. Ruellan A, Cavoret J, Ville F, Kleber X, Liatard B. Understanding white etching cracks in rolling element bearings: state of art and multiple driver transposition on a twin-disc machine. *Proc Inst Mech Eng Part J: J Eng Tribol*. 2017;231(2):203-220.
13. Röder J, Jacobs G, Duda T, Bosse D, Herzog F. Simulative investigation of wind turbine gearbox loads during power converter fault. *Forschung im Ingenieurwesen*. 2021;85(2):251-256.
14. Röder J, Jacobs G, Duda T, Bosse D, Herzog F. Investigation of dynamic loads in wind turbine drive trains due to grid and power converter faults. *Energies*. 2021;14(24):8542.
15. Eatherton S, Moroz E, Sadler D, Heidenreich D. Extreme torsional loads damage more than wind turbine gearboxes. 2016. https://www.windpowerengineering.com/extreme-torsional-loads-damage-more-than-wind-turbine-gearboxes/
16. Scherb BJ, Zech J. *A Study on the Smearing and Slip Behaviour of Radial Cylindrical Roller Bearings*, Georg-Simon-Ohm-Fachhochschule, Nürnberg: Georg-Simon-Ohm-Fachhochschule; 2001. https://books.google.se/books?id=Uvp9uAAACAAJ
17. Fowell M, Ioannides S, Kadiric A. An experimental investigation into the onset of smearing damage in nonconformal contacts with application to roller bearings. *Tribol Trans*. 2014;57(3):472-488.
18. Fateh F, White WN, Gruenbacher D. Torsional vibrations mitigation in the drivetrain of dfig-based grid-connected wind turbine. *IEEE Trans Industry Appl*. 2017;53(6):5760-5767.
19. Lee H, Han Y, Kim B. Attenuation of torsional vibration in the drivetrain of a wind turbine using a centrifugal pendulum absorber. In: Inter-Noise and Noise-Con Congress and Conference Proceedings, Vol. 263 Institute of Noise Control Engineering; 2021:3545-3553.

10991824, 0, Downloaded from https://onlinelibrary.wiley.com/doi/10.1002/we.2842 by Chalmers University Of Technology, Wiley Online Library on [19/06/2023]. See the Terms and Conditions (https://onlinelibrary.wiley.com/terms-and-conditions) on Wiley Online Library for rules of use; OA articles are governed by the applicable Creative Commons License

20. Peng J, Bian Y, Tian D, Liu P, Gao Z. Vibration alleviation for wind turbine gearbox with flexible suspensions based on modal interaction. *J Low Freq Noise, Vibr Active Control*. 2023. doi:10.1177/14613484221145183
21. Jonkman JM, Buhl Jr ML. Fast user's guide. Technical Report No. NREL/EL-500-38230, Golden, CO, National Renewable Energy Laboratory; 2005.
22. Jonkman J, Butterfield S, Musial W, Scott G. Definition of a 5-mw reference wind turbine for offshore system development. tech. rep., Golden, CO (United States), National Renewable Energy Lab.(NREL); 2009.
23. Vestas Wind Systems A/S. General specification V90-1.8/2.0 MW 50 Hz VCS. 2010. Accessed April 23, 2021. http://ventderaison.eu/gembloux/eie_ABO-WIND/Annexes/Annexe_N_1_Courbe_acoustique_V90.pdf
24. SIMPACK 2020x.2. 2020. Accessed November 11, 2021. https://www.3ds.com/products-services/simulia/products/simpack/
25. Abu-Rub H, Malinowski M, Al-Haddad K. *Power Electronics for Renewable Energy Systems, Transportation and Industrial Applications*: John Wiley & Sons; 2014.
26. Abad G, Lopez J, Rodriguez M, Marroyo L, Iwanski G. *Doubly Fed Induction Machine: Modeling and Control for Wind Energy Generation*: John Wiley & Sons; 2011.
27. NREL. *OpenFAST v3.0.0*: GitHub; 2021. Accessed February 3, 2022. https://github.com/OpenFAST/openfast/releases/tag/v3.0.0/
28. Girsang IP, Dhupia JS, Muljadi E, Singh M, Pao LY. Gearbox and drivetrain models to study dynamic effects of modern wind turbines. *IEEE Trans Industry Appl*. 2014;50(6):3777-3786.
29. Den Hartog JP. *Mechanical Vibrations*. Courier Corporation; 1985.
30. Zheng K, Yao Y, Shen T, Hikiri K, Sasaki M. Modeling and control of regenerative braking system in heavy duty hybrid electrical vehicles. In: 2008 SAE International Powertrains, Fuels and Lubricants Congress SAE; 2008;1-1569. https://www.sae.org/content/2008-01-1569/
31. Satzger C, de Castro R. Predictive brake control for electric vehicles. *IEEE Trans Vehic Technol*. 2017;67(2):977-990.
32. Satzger C, de Castro R, Bünte T. A model predictive control allocation approach to hybrid braking of electric vehicles. In: 2014 IEEE Intelligent Vehicles Symposium Proceedings IEEE; 2014:286-292.
33. Cerdeira-Corujo M, Costas A, Delgado E, Barreiro A, Banos A. Gain-scheduled wheel slip reset control in automotive brake systems. In: 2016 International Symposium on Power Electronics, Electrical Drives, Automation and Motion (SPEEDAM). IEEE; 2016:1255-1260.
34. GL D. DNVGL-ST-0437: loads and site conditions for wind turbines. 2016. https://www.dnv.com/energy/standards-guidelines/dnv-st-0437-loads-and-site-conditions-for-wind-turbines.html
35. Commission IE, et al. Wind turbines-part 1: design requirements. IEC 61400-1 Ed. 3; 2005.
36. HD860 series hydraulic disc brakes. Accessed September 14, 2022. https://www.axletech.com/en/products/brakes/hd860
37. Hydraulic fixed caliper disc brakes. Accessed September 14, 2022. https://www.knott.de/en/business-units/brakes-technology/disc-brakes

How to cite this article: Sarkar S, Johansson H, Berbyuk V. Mitigation of transient torque reversals in indirect drive wind turbine drivetrains. *Wind Energy*. 2023;1-23. doi:10.1002/we.2842

APPENDIX A: DERIVATION OF A SIMPLIFIED DRIVETRAIN MODEL COUPLED WITH A TORSIONAL TMD

For the drivetrain in Figure 6, it is assumed that the rotor is rotating at a constant speed Ω and the generator rotation can be obtained as

$$\begin{aligned} q_{rot} &= \Omega t \\ q_{gen} &= \Omega t + q_r \end{aligned} \tag{A1}$$

where q_r is the relative rotation between the rotor and the generator due to the elasticity of the shaft. This assumption reduces the degrees of freedom from $q = [q_{rot}, q_{gen}, q_d]$ to $q = [q_r, q_d]$. The equations of motion of this resulting 2-DOF system can be derived using the Euler–Lagrangian formalism as

$$\begin{bmatrix} J_{gen}^{eff} + J_{TMD}^{eff} & J_{TMD}^{eff} \\ J_{TMD}^{eff} & J_{TMD}^{eff} \end{bmatrix} \begin{pmatrix} \ddot{q}_r \\ \ddot{q}_d \end{pmatrix} + \begin{bmatrix} k_{eff} & 0 \\ 0 & k_{TMD}^{eff} \end{bmatrix} \begin{pmatrix} q_r \\ q_d \end{pmatrix} = \begin{pmatrix} \tau_r \\ 0 \end{pmatrix} \tag{A2}$$

where

$$\begin{aligned} J_{gen}^{eff} &= J_{PC} + N_1^2(J_S + J_{G1} + N_2^2(J_{G2} + J_{G3} + N_3^2(J_{G4} + J_{gen}))) \\ \frac{1}{k_{eff}} &= \frac{1}{k_{MS}} + \frac{1}{N_1^2 k_{LSS}} + \frac{1}{(N_1N_2)^2 k_{ISS}} + \frac{1}{(N_1N_2N_3)^2 k_{HSS}} \\ J_{TMD}^{eff} &= N^2 J_{TMD} \\ k_{TMD}^{eff} &= N^2 k_{TMD} \end{aligned} \tag{A3}$$

The equations of motion are then normalized by J_{gen}^{eff}, and the Rayleigh damping term is added to the equations of motion.

10991824, 0, Downloaded from https://onlinelibrary.wiley.com/doi/10.1002/we.2842 by Chalmers University Of Technology, Wiley Online Library on [19/06/2023]. See the Terms and Conditions (https://onlinelibrary.wiley.com/terms-and-conditions) on Wiley Online Library for rules of use; OA articles are governed by the applicable Creative Commons License

$$\begin{bmatrix} 1+\mu & \mu \\ \mu & \mu \end{bmatrix} \begin{pmatrix} \ddot{q}_r \\ \ddot{q}_d \end{pmatrix} + \begin{bmatrix} 2\zeta_n\omega_n & 0 \\ 0 & 2\zeta_d\omega_r\omega_n\mu \end{bmatrix} \begin{pmatrix} \dot{q}_r \\ \dot{q}_d \end{pmatrix} + \begin{bmatrix} \omega_n^2 & 0 \\ 0 & \mu\omega_r^2\omega_n^2 \end{bmatrix} \begin{pmatrix} q_r \\ q_d \end{pmatrix} = \begin{pmatrix} \overline{\tau}_r \\ 0 \end{pmatrix} \tag{A4}$$

The resulting equations of motion represent a primary system coupled to a TMD. Therefore, the classical Den Hartog formula[29] can be used to tune the TMD to the eigenfrequency of the primary system can be obtained as

$$\omega_n = \sqrt{k_{eff}\left[\frac{1}{J_{rot}} + \frac{1}{J_{gen}^{eff}}\right]} \tag{A5}$$

TABLE A1 Generic 2MW wind turbine specifications.

Class	IEC IIA
Rotor	
Diameter	90 m
Swept area	6362 m^2
Rated rotational speed	14.75 RPM
Rotational speed range	9.6–17.0 RPM
Cut-in, cut-out wind speeds	3.5 m/s, 25 m/s
Rotational direction	Clockwise (from front)
Type	Upwind
Tilt	6°
Cone	2°
Number of blades	3
Aerodynamic brakes	Full feathering
Blades	
Length	44 m
Maximum cord length	3.512 m
Blade tip cord	0.391 m
Twist at the root	27°
Approximate weight	6750 kg
Gearbox	
Type	1 planetary stage + 2 helical stages
Ratio	113.88
Tower	
Type	Conical tubular
Hub height	80 m
Weight	125 metric tonnes
Generator 2.0 MW	
Type	Asynchronous, wound rotor, slip rings and VCS
Rated power	2.0 MW
Frequency	50 Hz
Voltage, Generator	690 Vac
Number of poles	4
Approximate weight	7500 kg
Converter 2.0 MW	
Rated slip	12%
Rated RPM	1680 RPM
Rated rotor power (@ rated slip)	214 kW

10991824, 0, Downloaded from https://onlinelibrary.wiley.com/doi/10.1002/we.2842 by Chalmers University Of Technology, Wiley Online Library on [19/06/2023]. See the Terms and Conditions (https://onlinelibrary.wiley.com/terms-and-conditions) on Wiley Online Library for rules of use; OA articles are governed by the applicable Creative Commons License

TABLE A2 Gear data.

Gear	Type (mm)	Normal module (°)	Normal pressure angle (°)	Helix angle	No of teeth (mm)	Flank width (mm)
Planet	Internal	16	20	6	35	320
Sun	Internal	16	20	6	19	320
Ring	External	16	20	6	89	320
Gear 1	Internal	12	20	10	85	215
Pinion 1	Internal	12	20	10	19	215
Gear 2	Internal	6.5	20	16.5	103	150
Pinion 2	Internal	6.5	20	16.5	23	150

TABLE A3 Bearing data.

Name	Type	Model	No of rows	Roller diameter (mm)	Effective roller length (mm)	No of rollers	Pitch radius (mm)	Contact angle (°)
INP A	Spherical	241/600 ECAK30/W33	2	101.4	148.4	21	398.4	13
INP B	Spherical	241/530 ECAK30/W33	2	90.0	132.8	21	352.8	13
PLC A	Cylindrical	NCF 18/560 V/HB1	1	32.0	30.0	61	311.5	–
PLC B	Cylindrical	NCF 2984 V	1	38.0	62.0	40	243.0	–
PLx A/B	Cylindrical	NU 2344 ECMA	2	68.0	101.7	14	172.5	–
LSS A	Spherical	23984 CC/W33	2	32.5	37.8	40	247.4	6
LSS B	Spherical	23992 CAK/W33	2	37.5	43.0	38	272.6	6
IMS A	Cylindrical	NU 2338 ECML	1	60.0	95.5	13	150.0	–
IMS B	Cylindrical	NU 2340 ECML	1	62.0	100.0	13	157.5	–
IMS C	Ball	QJ 338 N2MA	1	63.5	–	12	147.5	35
HSS A	Cylindrical	NU 2234 ECML	1	38.0	62.0	16	121.5	–
HSS B	Cylindrical	NU 232 ECM	1	32.0	32.0	19	113.5	–
HSS C	Ball	QJ 328 N2MA	1	47.6	–	12	110.0	35

TABLE A4 Electrical parameters of the double fed induction generator model.[26]

Parameter	Value	Remark
Synchronous speed	1500 rpm	Synchronous speed at 50 Hz
Rated power	2 MW	Nominal stator three-phase active power
Rated stator voltage	690 V_{rms}	Line-to-line nominal stator voltage
Rated stator current	1760 A_{rms}	Each phase nominal stator current
Rated torque	12.7 kNm	Nominal torque
p	2	Number of pole pairs
u	1/3	Stator/rotor turn ratio
R_s	2.6 mΩ	Stator resistance
$L_{\sigma s}$	87 μH	Stator leakage inductance
L_m	2.5 mH	Magnetizing inductance
R'_r	26.1 mΩ	Rotor resistance
$L'_{\sigma r}$	783 μH	Rotor leakage inductance
R_r	2.9 mΩ	Rotor resistance referred to the stator
$L_{\sigma r}$	87 μH	Rotor leakage inductance referred to the stator
L_s	2.587 mH	Stator inductance, $L_s = L_m + L_{\sigma s}$
L_r	2.587 mH	Rotor inductance, $L_r = L_m + L_{\sigma r}$

10991824, 0, Downloaded from https://onlinelibrary.wiley.com/doi/10.1002/we.2842 by Chalmers University Of Technology, Wiley Online Library on [19/06/2023]. See the Terms and Conditions (https://onlinelibrary.wiley.com/terms-and-conditions) on Wiley Online Library for rules of use; OA articles are governed by the applicable Creative Commons License